

Dense Molecular Gas Associated with the Circumnuclear Star Forming Ring in the Barred Spiral Galaxy NGC 6951

Kotaro Kohno¹

Department of Astronomy, School of Science, The University of Tokyo
Bunkyo-ku, Tokyo, 113-0033, Japan

Ryohei Kawabe, and Baltasar Vila-Vilaró

Nobeyama Radio Observatory
Minamimaki, Minamisaku, Nagano, 384-1305, Japan

ABSTRACT

We present high resolution ($3'' - 5''$) observations of CO(J=1–0) and HCN(J=1–0) emission from the circumnuclear star forming ring in the barred spiral galaxy NGC 6951, a host of a type-2 Seyfert nucleus, using the Nobeyama Millimeter Array and the Nobeyama 45 m telescope.

We find that the distribution of the HCN emission is different from that of CO in the circumnuclear region of NGC 6951; it is confirmed that CO emission is dominated by “twin peaks” morphology with two spiral arms, which are connected to the dust lanes, as reported by Kenney et al. (1992). On the other hand, although the HCN emission also shows a twin peaks morphology, the HCN peaks are spatially shifted downstream compared with the CO peaks. Most of the HCN emission is associated with the circumnuclear ring, where vigorous star formation occurs. The HCN to CO integrated intensity ratio in the brightness temperature scale, $R_{\text{HCN/CO}}$, is also enhanced in the star forming ring. The peak value of the $R_{\text{HCN/CO}}$ is about 0.16 – 0.18, which is comparable to the $R_{\text{HCN/CO}}$ in the starburst regions of NGC 253 and M82. Consequently, the HCN emission spatially correlates better with the massive star forming regions than the CO emission in the circumnuclear region of NGC 6951.

The formation mechanism of dense molecular gas has been investigated. No significant enhancement of $R_{\text{HCN/CO}}$ is observed at the CO peaks, which are interpreted as x_1/x_2 orbit crowding regions. This suggests that the shocks along the orbit crowding do not promote the formation of dense molecular gas effectively but enhance the presence of low density GMCs in NGC 6951. Instead, gravitational instability can account for the dense molecular gas formation in the circumnuclear star forming ring because Toomre’s Q value is below unity there.

¹present address: Nobeyama Radio Observatory, e-mail: kotaro@nro.nao.ac.jp

The $R_{\text{HCN/CO}}$ toward the type-2 Seyfert nucleus of NGC 6951 is 0.086 averaged over central $r < 120$ pc region. This is a rather normal value compared with non-active galaxies such as the Milky Way, and quite different from other type-2 Seyfert galaxies NGC 1068 and M51 where extremely high $R_{\text{HCN/CO}}$ of ~ 0.5 have been reported. The variety of $R_{\text{HCN/CO}}$ values in these Seyfert nuclei would be attributed to the different physical conditions of the molecular gas around the nuclei.

Subject headings: galaxies: individual (NGC 6951) — galaxies: ISM — galaxies: kinematics and dynamics — galaxies: Seyfert — galaxies: starburst

1. Introduction

Observational studies of molecular gas in the Milky Way have clearly shown that stars are formed from dense cores of molecular clouds rather than their diffuse envelopes (e.g. Lada 1992). Hence it is essential to study the properties of dense molecular gas in order to understand star formation in galaxies, and particularly starburst phenomena.

Dense molecular material is investigated by observing the molecules referred as “high density tracers”, which require larger hydrogen density than that of CO for their collisional excitation, such as HCN, HCO^+ , CS, and so on (e.g. Mauersberger & Henkel 1989; Sage, Shore, & Solomon 1990; Henkel, Baan, & Mauersberger 1991; Nguyen-Q-Rieu et al. 1992; Solomon et al. 1992; Helfer & Blitz 1993; Aalto et al. 1995; Paglione et al. 1995; Paglione, Jackson, & Ishizuki 1997). For example, CO(1–0) emission is excited even in low density molecular gas ($n_{\text{H}_2} \sim 500 \text{ cm}^{-3}$), whereas HCN(1–0) emission traces very dense molecular clouds ($n_{\text{H}_2} > 10^4 \text{ cm}^{-3}$) due to its quite larger dipole moment ($\mu_{\text{HCN}} = 3.0$ Debye, whereas $\mu_{\text{CO}} = 0.10$ Debye).

Observational evidence suggesting a close relationship between dense molecular gas and massive star formation in various galaxies has been accumulated in recent years; Solomon et al. (1992) reported a tight correlation between the HCN(1–0) and far-infrared luminosity in 12 galaxies, suggesting that the star formation rate is tightly related to the amount of the dense molecular gas measured by HCN emission. This study has been expanded to larger samples (Gao & Solomon 1996). It has been also claimed that the HCN luminosity correlates with the $\text{H}2\alpha$ recombination line luminosity, which is another tracer of massive star formation (Zhao et al. 1996). It is then natural to expect that dense molecular gas has a similar spatial distribution as that of the massive star forming regions. Indeed, a rough association between dense molecular complexes and star forming regions traced by radio continuum emission has been observed in the prototypical starbursts M82 (Shen & Lo 1995; Golla, Allen, & Kronberg 1996) and NGC 253 (Paglione, Tosaki, & Jackson 1995). However, there are contradicting results on HCN – FIR correlation (e.g. Aalto et al. 1995), and only a few galaxies till present have been mapped in HCN emission with enough high spatial resolution to compare with the massive star forming regions. It is therefore necessary to observe HCN emission from the galaxies which have extended massive star forming regions.

The formation mechanism of dense molecular clouds is another important issue. At large spatial scales, gravitational instabilities of the molecular gas (e.g. Kennicutt 1989; Elmegreen 1994) and the shocks associated with the orbit crowdings (e.g. Combes & Gerin 1985) are thought to be responsible for the dense gas formation. Closer to the centers of galaxies, Inner Lindblad Resonances (ILRs) are considered to be essential to explain the distribution and kinematics of molecular gas as well as star formation (e.g. Kenney et al. 1992; Telesco, Dressel, & Wolstencroft 1993; Sakamoto et al. 1995), and therefore dense gas cloud formation.

In order to address the issues described above, we observed CO(1–0) and HCN(1–0) emission in the central region of a nearby barred spiral galaxy, NGC 6951, using the Nobeyama Millimeter Array (NMA) and the Nobeyama 45 m telescope ². Optical and radio observations indicate a vigorous star formation in the circumnuclear region of this galaxy. Both H α (Márquez & Moles 1993; Wozniak et al. 1995; Rozas, Beckman, & Knapen 1996; González-Delgado et al. 1997) and 6 cm radio continuum emission (Vila et al. 1990; Saikia et al. 1994) are mainly concentrated in the central (a few hundred parsec) region of NGC 6951, indicating that most of the star formation occurs in a circumnuclear ring structure (Fig. 1). The diameter of this circumnuclear star forming ring is about $6'' \times 9''$ (e.g. Barth et al. 1995; Buta & Crocker 1993). The star formation rate of the ring estimated from the H α luminosity is $\sim 4 M_{\odot} \text{ yr}^{-1}$ after correction for internal extinction (Table 1), and is comparable to those in the central regions of nearby starburst galaxies, though the gas consumption timescale due to star formation is fairly longer than those in starbursts (Kenney 1997). We can therefore resolve spatially the distribution of dense molecular gas using a millimeter-wave interferometer, and compare it with the extent of the vigorous star forming regions. Near-infrared photometry has revealed the presence of a large stellar bar with a semimajor radius of $\sim 44''$ (Mulchaey, Regan, & Kundu 1997; Friedli et al. 1996; Elmegreen et al. 1996), which corresponds to ~ 5 kpc at the adopted distance of $D = 24.1$ Mpc. Optical images show two straight dust lanes along the bar (Kenney et al. 1992; Márquez & Moles 1993; Wozniak et al. 1995) which trace the shock front at the leading edges of the bar as predicted from numerical simulations (Robert, Huntley, & van Albada 1979; Athanassoula 1992). CO(1–0) emission has been mapped with the Caltech millimeter array (Kenney et al. 1992) and show a “twin peaks” morphology. The positions of the ILRs deduced from their CO rotation curve indicate that the two-armed CO peaks would be explained as a result of orbit crowding near the outer ILR (OILR). Therefore, this circumnuclear ring of NGC 6951 provides us with an unique opportunity to investigate the relationship between the spatial variations of the physical conditions of molecular gas and its dynamics, especially concerned orbit resonances and associated shocks.

In addition to the study of the star forming activity, in this object we can also address the relationship between an AGN and molecular gas properties, because this galaxy hosts an active nucleus (type-2 Seyfert; Boer & Schulz 1993; Ho, Filippenko, & Sargent 1995). As it has been

²Nobeyama Radio Observatory is a branch of the National Astronomical Observatory, an inter-university research institute, operated by the Ministry of Education, Science, Sports and Culture, Japan.

reported in the recent literature, there seems to be a striking enhancement of the integrated HCN(1–0) to CO(1–0) intensity ratio in brightness temperature scale (hereafter $R_{\text{HCN/CO}}$) toward the type-2 Seyfert nucleus of NGC 1068 (Jackson et al. 1993; Tacconi et al. 1994; Helfer & Blitz 1995) and the low-luminosity active galactic nucleus in M51 (Kohno et al. 1996; Matsushita et al. 1998); the $R_{\text{HCN/CO}}$ is as high as ~ 0.5 toward these two Seyfert nuclei. These high $R_{\text{HCN/CO}}$ values in a few hundred parsec scale region have never been found anywhere in the Milky Way, implying extreme conditions of the molecular gas in the circumnuclear region of Seyfert galaxies. It is therefore quite exciting to explore whether such an extremely high $R_{\text{HCN/CO}}$ is common or not in the circumnuclear regions of Seyfert galaxies.

An $\text{H}\alpha + [\text{NII}]$ contour map (Wozniak et al. 1995) superposed on an optical broad band image of NGC 6951 is shown in Fig. 1, together with the area observed with the NMA. The properties of NGC 6951 were summarized in Table 1. In this paper we adopt a distance of NGC 6951 of 24.1 Mpc (Tully 1988), which agrees well with that estimated using the Tully-Fisher relationship, 23.4 Mpc (Bottinelli et al. 1984; see also Márquez & Moles 1993).

We describe the observational parameters and results in Section 2, and present new CO and HCN data of NGC 6951 in Section 3, which reveal the different distribution of HCN emission from CO, namely, the spatial variation of physical condition in the circumnuclear molecular clouds. With these data, we discuss about the possible cause of the variation and its relationship to the central activity of NGC 6951 in Section 4. Finally we summarize the conclusions of this study in Section 5.

2. Observations

2.1. Nobeyama Millimeter Array

The central region of NGC 6951 was observed in the J=1–0 line of CO and HCN with the NMA. The NMA consists of six 10 m dishes providing 15 baselines simultaneously. The observations were made during November 1995 to February 1996 in the three available array configurations (AB, C, & D). Due to the limitation of the minimum projected baseline length (10 m), extended structures larger than about $50''$ in each channel map are not sampled in the observations. The front-end are tunerless SIS receivers, whose receiver temperature is ~ 50 K in double side band, and the typical system noise temperature (in single side band) were 300 – 600 K for the HCN observations and 400 – 800 K for CO the observations. A digital spectro-correlator FX was configured to cover 320 MHz with 1024 channels per baseline. Sideband separation was achieved by 90° phase switching. We observed a radio source 3C418 for 5 minutes every 30 minutes in order to calibrate temporal variations of the visibility amplitude and phase. The passband across 1024 channels was calibrated through observations of strong continuum sources 3C273 and NRAO 530. The flux density of the reference calibrator 3C418 was measured at 88 GHz from comparisons with planets of known brightness temperatures. The flux density of 3C418 at 114

GHz (CO observations) was estimated by an extrapolation of its spectrum assuming a spectral index of -0.34 which was derived from the flux at 88 GHz and the lower frequency fluxes listed in the VLA calibrator database. The uncertainty in the absolute flux scale is $\sim \pm 20\%$.

The raw data were calibrated and edited using the package UVPROC-II developed at NRO and Fourier transformed with natural uv weighting with the NRAO AIPS. A conventional CLEAN method was applied to deconvolve the synthesized beam pattern. We made CO channel maps with a synthesized beam of $3''.9 \times 3''.1$ at a velocity width of 9.79 km s^{-1} , and HCN channel maps with a synthesized beam of $4''.7 \times 4''.5$ at 38.21 km s^{-1} velocity width every 19.11 km s^{-1} were made. The typical noise levels of channel maps are 34 mJy beam^{-1} ($= 260 \text{ mK in } T_b$) for CO and $5.1 \text{ mJy beam}^{-1}$ ($= 37 \text{ mK}$) for the HCN data, respectively. Parameters of the NMA observations described above are summarized in Table 2.

We searched continuum emission by binning-up line free channels of the HCN observations, but did not find any. No subtraction of continuum emission was therefore needed for the channel maps. The 2σ upper limit of the 3.4 mm continuum emission is $2.4 \text{ mJy beam}^{-1}$ (beam size $5''.4 \times 5''.0$ for this continuum search) within the observed field.

2.2. NRO 45 m telescope

In order to evaluate the missing flux of the interferometry, we obtained single dish CO and HCN spectra toward the center of NGC 6951 using the NRO 45 m telescope. The observations were carried out in May 1996. In order to avoid the degradation of the beam pattern, aperture efficiency, and pointing accuracy of the telescope, we used only the data taken when wind velocity was less than 5 m s^{-1} . The full half-power beam width, aperture efficiency, and main-beam efficiency were measured to be $15''$ ($19''$), 0.37 ± 0.02 (0.44 ± 0.02), and 0.45 ± 0.03 (0.50 ± 0.03) at the observed frequency of CO (HCN), respectively. We used two cooled SIS mixer receivers equipped with sideband rejection filters and observed both CO and HCN line simultaneously. The beam squint of the two receivers had been aligned to less than $2''$. Absolute pointing of the antenna was checked every hour using the SiO maser source T-Cep at 43 GHz, and was measured as accurate as $\sim 2''$ rms. System noise temperature for CO and HCN observations were typically 750 K and 350 K in single side band, respectively. Sky emission were subtracted by position switching with two off-source positions at offsets in azimuth of $\pm 5'$ from the observed position. Spectra of CO and HCN emission were obtained with 2048 channels acousto-optical spectrometers of 250 MHz bandwidth, corresponding to a velocity coverage of 650 km s^{-1} for CO observations, and 850 km s^{-1} for HCN observations. Only linear baselines were removed from the spectra and adjacent channels were binned to a velocity resolution of 10 km s^{-1} and 20 km s^{-1} for CO and HCN spectra, respectively. The resultant noise level of the CO spectrum was $9.5 \text{ mK rms in } T_A^*$ scale and 2.4 mK rms for the HCN spectrum.

3. Results

3.1. Distribution of Molecular Gas

3.1.1. Channel maps, profile maps, and integrated intensity

Fig. 2 shows the channel maps of the CO emission and HCN emission in the central $30'' \times 30''$ region ($3.5 \text{ kpc} \times 3.5 \text{ kpc}$) of NGC 6951. We detected significant ($> 3 \sigma$) CO emission in 40 adjacent channels with a velocity range of $V_{\text{LSR}} = 1214 - 1594 \text{ km s}^{-1}$. This velocity width (full width of zero intensity) of 390 km s^{-1} is almost the same as that of single-dish line profiles obtained with the FCRAO 14 m (Young et al. 1995). HCN emission was detected ($> 3 \sigma$) over a velocity range of $V_{\text{LSR}} = 1225 - 1567 \text{ km s}^{-1}$, which is almost the same as that of the CO line. Note that this is the first measurement of HCN emission from NGC 6951. It is noteworthy that both CO and HCN emission are weak near the systemic velocity ($V_{\text{LSR}} \sim 1428 \text{ km s}^{-1}$; Table 4), indicating that neither CO nor HCN emission show significant concentration toward the Seyfert nucleus of NGC 6951.

The velocity-integrated intensity maps of the CO and HCN emission are shown in Fig. 3, together with the CO and HCN line profile maps. These images were made by the calculation of the 0-th moment from the 3-dimensional data cube. To minimize the contribution from noise, we computed these moment maps with a clip level of 2σ for CO and 1.5σ for HCN in each channel maps.

3.1.2. 45m observations and flux measurements

Here we compare the CO and HCN flux from our NMA observations with single-dish observations in order to evaluate the missing flux of our interferometry. CO and HCN fluxes were measured by summing the emission from individual channel maps corrected for the primary beam attenuation.

The total CO flux within our field of view ($65''$) is $334 \pm 12 \text{ Jy km s}^{-1}$. On the other hand, CO flux from the central $45''$ diameter of NGC 6951 was measured to be $350 \pm 41 \text{ Jy km s}^{-1}$ with the FCRAO 14 m telescope (Young et al. 1995). Because most of the CO emission in our NMA observations are confined within the central $45''$ diameter (i.e. beam size of the FCRAO 14 m), it seems that most of the single-dish flux is sampled in our NMA observations. Note that low level CO emission has been detected over the disk of NGC 6951 (Kuno et al. 1997), and our interferometric observations may have missed these weak extended emission.

We detected a total HCN flux of $18.7 \pm 1.9 \text{ Jy km s}^{-1}$ inside our field of view ($84''$). Since there are no data for HCN flux observed with any 10 m class single-dish telescope, we convolved our HCN data cube to $19''$ resolution and compared them with the 45 m spectrum. Fig. 4 shows the profiles of CO and HCN emission in main-beam temperature scale $T_{\text{MB}} = T_{\text{A}}^*/\eta_{\text{MB}}$. We find

that both the CO and HCN emission profiles from our 45 m observations agree very well with the convolved NMA profiles, indicating that both CO and HCN maps from the NMA seems to recover almost all of single-dish flux again, and that we can safely discuss the distribution, kinematics, and line ratio of molecular gas below. Note that the moment maps in the following figures recovers about 70 – 90 % of single dish flux because these maps are made with a clipping of low-level emission. All flux measurements, including line ratio calculation, are from the maps without clippings. Attenuation due to the primary beam pattern of 10 m dish is also corrected for these flux measurements. The summary of 45 m observations are listed in Table 3.

3.1.3. *Distribution of CO and HCN emission*

Fig. 5 shows the spatial relationship between molecular gas, dust lanes, and the circumnuclear star forming ring traced by H α emission (Wozniak et al. 1995) and the 6 cm radio continuum emission (Saikia et al. 1994). CO emission in the central region of NGC 6951 is confirmed to be dominated by two strong peaks on spiral arms (hereafter the CO arms), referred as “twin-peaks” by Kenney et al. (1992), which are directly connected to the dust lanes along the bar. The inner part of the two CO arms corresponds to the circumnuclear star forming ring. These features agree well with the previously reported one (Kenney et al. 1992). On the other hand, as it can be clearly seen in Fig. 5, *the distribution of the HCN emission is significantly different to that of CO*. First, though the HCN emission also shows a twin peak morphology, the peaks are spatially shifted from those of CO. If we assume that the spiral arms of NGC 6951 seen in optical images (Fig. 1) are trailing as in case of almost all spiral galaxies, the rotation is clockwise as indicated by an arrow in the figure and the HCN emission is shifted downstream. Moreover, the HCN peaks are located closer to the nucleus than the CO peaks. About 44 % of the total CO flux comes from the ring ($r < 6''$), whereas 60 % of the HCN emission is associated with it. Namely, *the HCN emission correlates better spatially with the massive star forming region than the CO emission in NGC 6951*. Although the presence of a strong and non-uniform extinction is reported from the H α /H β ratio variations across the ring (Barth et al. 1995), both H α and radio continuum show good agreement with the HCN emission.

Association between the HCN distribution and the massive star forming regions has been reported in prototypical starburst galaxies M 82 (Shen & Lo 1995; Golla et al. 1996) and NGC 253 (Paglione et al. 1995), although these are edge-on galaxies. Dense molecular gas is also distributed in the starburst ring (or arms) of NGC 1068 (Jackson et al. 1993; Helfer & Blitz 1995). Particularly, sensitive observations with the PdB interferometer have clearly depicted the HCN emission associated with the starburst ring of NGC 1068 (Tacconi et al. 1994), which is quite similar to the case of the circumnuclear star forming ring of NGC 6951. The HCN distribution of IC 342 (Downes et al. 1992) may also be an example of such coincidence ³.

³Although Downes et al. (1992) states that neither CO nor HCN trace star formation in IC 342, the HCN emission

We note that the FIR/HCN luminosity ratio $L_{\text{FIR}}/L'_{\text{HCN}}$ in NGC 6951 is about 400 (Table 2), which is similar to the values in ultra-luminous IR galaxies, whereas $L_{\text{FIR}}/L'_{\text{CO}} \sim 40$ is about 5 times smaller than those in ultra-luminous IR galaxies (Solomon et al. 1992). These comparisons support the results of Solomon et al. (1992), which have shown that $L_{\text{FIR}}/L'_{\text{HCN}}$ is independent of the L_{FIR} , whereas $L_{\text{FIR}}/L'_{\text{CO}}$ increases with L_{FIR} .

Interestingly, there is no central peak in HCN emission. This is different from the other Seyfert galaxies NGC 1068 and M51, where there is a strong concentration of HCN emission toward the nucleus, in spite of weak or no CO peak there (Jackson et al. 1993; Tacconi et al. 1994; Helfer & Blitz 1995; Kohno et al. 1996).

3.1.4. Molecular gas mass and surface density

The mass of molecular gas is estimated from the CO emission assuming the Galactic $I(\text{CO})$ to $N(\text{H}_2)$ conversion factor. Adopting a conversion factor of $X_{\text{CO}} = 3 \times 10^{20} \text{ cm}^{-2} (\text{K km s}^{-1})^{-1}$ (Scoville et al. 1987; Solomon et al. 1987), the mass of molecular hydrogen is

$$M_{\text{H}_2} = 1.2 \times 10^4 \times \left(\frac{S(\text{CO})}{\text{Jy km s}^{-1}} \right) \left(\frac{D}{\text{Mpc}} \right)^2 M_{\odot}, \quad (1)$$

where $S(\text{CO})$ is the CO flux density. Taking into account that the mass of molecular contents including He and other elements as $M_{\text{gas}} = 1.36 \times M_{\text{H}_2}$, the total mass of molecular gas detected in our integrated intensity map is $3.2 \times 10^9 M_{\odot}$, and the molecular gas mass within $r < 6''$, the radius of the circumnuclear ring, is $1.4 \times 10^9 M_{\odot}$.

The surface mass density of molecular hydrogen on the galaxy plane is calculated as

$$\Sigma_{\text{H}_2} = 4.8 \times \cos(i) \times \left(\frac{I(\text{CO})}{\text{K km s}^{-1}} \right) M_{\odot} \text{ pc}^{-2}, \quad (2)$$

where i is the inclination of the galaxy ($i = 42^\circ$ for NGC 6951). In case of our CO observations, the 1σ level of CO integrated intensity map, $1.9 \text{ Jy beam}^{-1} \text{ km s}^{-1}$ or 15 K km s^{-1} , corresponds to a face-on molecular gas surface density $\Sigma_{\text{gas}} = 1.36 \times \Sigma_{\text{H}_2} = 73 M_{\odot} \text{ pc}^{-2}$, and the CO peak (27σ) is $2.0 \times 10^3 M_{\odot} \text{ pc}^{-2}$. Note that this gas surface density does not depend on the adopted distance to the galaxy.

mostly arises from a central ring where massive star formation occurs (Wright et al. 1993; Telesco et al. 1993; Böker, Förster-Schreiber, & Genzel 1997). On the other hand, a considerable fraction of the CO emission comes from the two bright ridges which extend for $\sim 30''$ from the nucleus (Ishizuki et al. 1990; see also the CO mosaic map in Wright et al. 1993). Accordingly, the HCN emission may correlate better spatially with the star formation than the CO emission in IC 342, as in the case of NGC 6951.

3.2. $R_{\text{HCN}/\text{CO}}$ ratio

CO(1–0) emission is excited even in low density molecular gas ($n_{\text{H}_2} \sim 500 \text{ cm}^{-3}$) whereas HCN(1–0) emission traces very dense molecular clouds ($n_{\text{H}_2} > 10^4 \text{ cm}^{-3}$). Therefore the comparison of CO and HCN intensity is a measure of gas density if both CO and HCN emission come from the same volume. Fig. 6 shows the dependence of $R_{\text{HCN}/\text{CO}}$ on kinetic temperature and density of molecular gas (Kohno 1998), which was computed employing the large velocity gradient approximation (Solomon & Scoville 1974; Goldreich & Kwan 1974)⁴. In case of external galaxies, observing beams are usually too large to distinguish the individual molecular cloud structures, and the one-zone assumption is no longer valid. Thus CO and HCN line intensity ratio is interpreted as the fraction of dense molecular gas to the total (including diffuse) molecular gas within the observing beam.

3.2.1. Distribution of $R_{\text{HCN}/\text{CO}}$

We convolved the CO map to the same beam size as that of the HCN map in order to compare directly the HCN and CO line intensities. Fig. 7(a) is a map of the HCN to CO integrated intensity ratio in brightness temperature scale ($R_{\text{HCN}/\text{CO}}$), and Fig. 7(b) is a comparison of the $R_{\text{HCN}/\text{CO}}$ with the 6 cm continuum emission (Saikia et al. 1994). It is immediately evident that $R_{\text{HCN}/\text{CO}}$ values are significantly enhanced in the 6 cm continuum peaks, where intense star formation occur. The highest value of $R_{\text{HCN}/\text{CO}}$ is about 0.16 – 0.18, which is similar to the ratios observed in the molecular gas in the nuclear starburst region of M82 and NGC 253 (Shen & Lo 1995; Paglione et al. 1995). We have also detected strong HCN emission toward the nucleus of the young starburst galaxy NGC 3504, where $R_{\text{HCN}/\text{CO}}$ exceeds 0.2 (Kohno et al. 1997). The Sgr-B2 cloud, a massive star forming region in the central region of the Milky Way, also has a very high $R_{\text{HCN}/\text{CO}}$ of ~ 0.2 (Jackson et al. 1996). On the other hand, an $R_{\text{HCN}/\text{CO}}$ of 0.16 – 0.18 is much larger than that observed in the Galactic disk, $R_{\text{HCN}/\text{CO}} \sim 0.026 \pm 0.008$ (Helfer & Blitz 1997b) and the central regions of “normal” galactic nuclei (which means the nuclei showing no extreme activities), such as Milky Way where a ratio ~ 0.08 is observed averaged over the central 600 pc region (Jackson et al. 1996; Helfer & Blitz 1997b).

Fig. 8 shows the azimuthally averaged radial profile of $R_{\text{HCN}/\text{CO}}$. Again, we can see that the ratio is enhanced at the circumnuclear star forming ring. The azimuthly averaged value of the $R_{\text{HCN}/\text{CO}}$ in the circumnuclear ring is 0.13. This is comparable to the azimuthally averaged $R_{\text{HCN}/\text{CO}}$ in the Starburst ring of NGC 1068, which is also as high as 0.1 (Helfer & Blitz 1995).

Turning now to the nucleus, we see that the $R_{\text{HCN}/\text{CO}}$ toward the type 2 Seyfert nucleus of

⁴ $R_{\text{HCN}/\text{CO}}$ values are often interpreted as a measure of thermal gas pressure (Helfer & Blitz 1997b; Paglione et al. 1998). However, gas pressure is expressed as a product of gas density and kinematic temperature, and is strongly dependent on the gas density (Fig. 6; see also Paglione et al. 1998)

NGC 6951 is 0.083 averaged over the central $r < 120$ pc region (Fig. 8). This ratio is a rather normal value compared with other non-active galaxies, and quite different from the previously studied Seyfert galaxies NGC 1068 and M51, where extremely high $R_{\text{HCN/CO}}$ of ~ 0.5 have been reported (Jackson et al. 1993; Tacconi et al. 1994; Kohno et al. 1996; Matsushita et al. 1998). We note that the lack of a central peak in $R_{\text{HCN/CO}}$ radial distribution is in contrast with the other galaxies; high resolution measurements of $R_{\text{HCN/CO}}$ in NGC 1068 (Helfer & Blitz 1995), M51 (Kohno et al. 1996) and NGC 6946 (Helfer & Blitz 1997a) have been shown centrally peaked $R_{\text{HCN/CO}}$ radial profile.

As a summary of this section, we present the CO, HCN, and $R_{\text{HCN/CO}}$ distribution in a polar coordinate graph. Fig. 9 shows the definition of the axis used to measure the radius R and the position angle ϕ , and Fig. 10 shows the maps. The features described above are also clearly revealed in these maps; the HCN emission and $R_{\text{HCN/CO}}$ peaks are shifted downstream with respect to the CO peaks. The difference of the position angle between the CO peaks and the $R_{\text{HCN/CO}}$ peaks is $\sim 50^\circ - 60^\circ$. Most of the HCN emission is associated with the star forming ring at a radius of $3'' \sim 6''$, whereas a considerable fraction of the CO emission originates from the two arms located beyond the ring ($r > 6''$). The peaks of $R_{\text{HCN/CO}}$ are coincided with the massive star formation traced by the 6 cm radio continuum emission, suggesting a tight relationship between dense molecular gas and vigorous star formation in NGC 6951.

3.2.2. Mass fraction of dense molecular gas

It may be meaningful to interpret $R_{\text{HCN/CO}}$ values as the mass fraction of dense molecular gas, $M_{\text{dense}}/M_{\text{total}}$, where M_{dense} is the mass of dense molecular gas traced by HCN(1–0), and M_{total} is the total mass (i.e. both dense and diffuse) of molecular gas traced by CO. M_{dense} can be estimated using an ‘‘HCN conversion factor’’, $X_{\text{HCN}} \equiv N(\text{H}_2)/L'(\text{HCN})$. X_{HCN} is computed to be $\sim 20 M_\odot (\text{K km}^{-1} \text{ pc}^2)^{-1}$ or $1.3 \times 10^{21} \text{ cm}^{-2} (\text{K km s}^{-1})^{-1}$, assuming that the HCN emission traces gas in gravitationally bound or virialized clouds (Solomon et al. 1992). Together with the adopted CO conversion factor here, $X_{\text{CO}} = 3 \times 10^{20} \text{ cm}^{-2} (\text{K km s}^{-1})^{-1}$, we find that $R_{\text{HCN/CO}} = 0.1$ corresponds to $M_{\text{dense}}/M_{\text{total}} = 43\%$. Accordingly, in starburst regions where high $R_{\text{HCN/CO}}$ values of ~ 0.2 are observed, $M_{\text{dense}}/M_{\text{total}}$ values may be close to $\sim 100\%$, i.e. the molecular gas mass is mostly dominated by the dense component. In the center of M82, a high fraction of dense molecular gas ($M_{\text{dense}}/M_{\text{total}} \sim 40\%$) has been estimated based on HCN (Boer & Schulz 1993) and high-J CO (Güsten et al. 1993) observations⁵. Note that the $M_{\text{dense}}/M_{\text{total}}$

⁵We would like to make a brief comment on the extremely high $R_{\text{HCN/CO}}$ values of ~ 0.5 toward some Seyfert nuclei such as NGC 1068 and M51. If we adopt the same X_{HCN} in these regions, it immediately results in an overestimation of dense molecular gas mass because $M_{\text{dense}}/M_{\text{total}}$ exceeds 100%. We suggest that X_{HCN} may have a significantly different value there; Kohno (1998) has examined the dependence of the X_{HCN} on the physical properties of gas based on the LVG model (Sakamoto 1997) and shown that X_{HCN} tends to increase under very high kinematical temperature ($T_{\text{kin}} > 100$ K) and high gas density ($n_{\text{H}_2} \sim 10^5 \text{ cm}^{-3}$) conditions. In fact, T_{kin} and n_{H_2} have been

values derived here could contain considerable errors mainly due to the uncertainties of both X_{HCN} and X_{CO} .

3.3. Kinematics of Molecular Gas

3.3.1. Velocity field

Fig. 11 shows an intensity-weighted isovelocity contour map of the CO emission. This map was made by computing the first moment of the CO data cube, as $\langle v \rangle = \Sigma v_i S_i / \Sigma S_i$. Circular motion dominates the kinematics in the central region of NGC 6951, however, we can see a “S-shape” twist of isovelocity contours near the systemic velocity, suggesting the existence of non-circular motions.

We determined the kinematical parameters of the circumnuclear molecular gas ring (dynamical center, position angle of the major axis, inclination angle, and systemic velocity) by a least square fitting of the intensity-weighted isovelocity field as a circular rotation. We used a fitting only to the central region ($1'' < r < 5''$) because the gas distribution is far from axisymmetric in the outer parts ($r < 6''$) and also large deviations from circular motion appear to exist there. The GAL package in AIPS was used for this analysis. The derived parameters are listed in Table 4. Note that these quantities may still contain systematic errors due to the presence of non-circular motions seen in the mean velocity map.

The position of the dynamical center determined from this observations roughly corresponds with the position of the Seyfert nucleus defined as the central peak of the 6 cm radio continuum (Saikia et al. 1994) within a difference smaller than $0''.5$. The systemic velocity is consistent with the H α observations, $V_{\text{hel}} = 1418 \pm 15 \text{ km s}^{-1}$ (Márquez & Moles 1993). The position angles of the major axis estimated from optical isophotal fits range from 138° (Márquez & Moles 1993) to 170° (RC3). The derived value from our CO data, $P.A.$ of 130° , favors the smallest one. The inclination angle was highly uncertain from the fitting, and we adopted the value determined by Márquez & Moles (1993).

Position - velocity diagrams (pv diagrams) along the major axis ($P.A. = 130^\circ$) of NGC 6951 are shown in Fig. 12. It is confirmed that the CO emission is weak toward the nucleus in the pv diagram along the major axis.

estimated to be $\sim 100 \text{ K}$ and $\sim 10^5 \text{ cm}^{-3}$, respectively, in the central regions of NGC 1068 (Tacconi et al. 1994) and M51 (Matsushita et al. 1998). Anyway, essentially *all* of the molecular gas must be dense in regions where very high $R_{\text{HCN/CO}}$ values are observed.

3.3.2. Rotation curve

Fig. 12(a) shows the rotation curve of the inner part of NGC 6951 obtained by averaging the intensity-weighted mean velocities (Fig. 11) within $\pm 5^\circ$ area of the major axis. It should be noted that the velocity field contains non-circular motions and the derived rotation curve must be treated as an averaged rotation curve, possibly with significant local deviations.

The dynamical mass within a radius r is calculated as

$$M_{\text{dyn}} = \frac{rv^2(r)}{G} = 2.3 \times 10^5 \times \left(\frac{r}{\text{kpc}}\right) \left(\frac{v(r)}{\text{km s}^{-1}}\right)^2 M_{\odot}, \quad (3)$$

assuming a spherical mass distribution and Keplerian rotation. The dynamical mass within the radius of $6''$ is then calculated as $4.9 \times 10^9 M_{\odot}$, so the ratio of dynamical mass to the total molecular gas mass $M_{\text{gas}}/M_{\text{dyn}}$ is about 29 % within the ring. This is a very high value, yet such large gas mass fraction is often observed in the central regions of galaxies (e.g. Turner 1994).

The angular velocity $\Omega(r) = v(r)/r$, epicyclic frequency $\kappa(r) = [2\{v(r)/r\}\{v(r)/r + dv(r)/dr\}]^{0.5}$, and $\Omega - \kappa/2$ calculated from the rotation curve, are shown in Fig. 13(b). ILRs will exist wherever $\Omega - \kappa/2$ exceeds the pattern speed of the bar Ω_{bar} at some location within corotation. The bar pattern speed (indicated as dashed line) was estimated to be $\sim 50 \text{ km s}^{-1} \text{ kpc}^{-1}$, assuming that corotation is located at the end of the bar. We took the bar radius as $44''$ from Mulchaey et al. (1997), and the rotation velocity at the bar end was derived from the H α data (Márquez & Moles 1993). It is evident that the bar pattern speed remains below $\Omega - \kappa/2$ within a radius of $\sim 800 \text{ pc}$. This is similar to the loci of the CO arms, $r \sim 6'' - 10''$, and roughly agrees with the analysis by Kenney et al. (1992). The inner ILR (IILR) should be located near the nucleus, however, we cannot elaborate on the location of the IILR accurately because our rotation curve in Fig. 13(a) is affected by limited angular resolution in the central parts (within $r \sim 400 \text{ pc}$).

3.3.3. Deviation from circular rotation

Since deviations from pure circular motion can be more clearly seen in velocity residual maps, a model velocity field derived from the rotation curve in Fig. 13(a) assuming pure circular motion was subtracted from the observed velocity field (Fig. 11). The resultant velocity residual map is shown in Fig. 14, overlaid on the CO intensity map (greyscale) and the position of the dust lanes (dashed lines).

This comparison shows that the largest deviations from circular motion occur at the end of the two CO arms which are directly connected to the dust lanes. If we assume that the spiral arms in NGC 6951 are trailing, then these dust lanes are located at the leading sides of the bar, and the southwestern part of the galaxy is the near side, indicating that the deviations associated with the dust lanes seen in Fig. 14 could be radial inflowing motion along the bar, as predicted

by theory (Roberts et al. 1979; Athanassoula 1992). This feature has been reported in barred spiral galaxies such as NGC 4314 (Benedict, Smith, & Kenney 1996) and NGC 1530 (Reynaud & Downes 1997). Inside the ring, the spiral dust lane pattern has been reported (Barth et al. 1995) and it is also important to know whether the gas near the Seyfert nucleus of NGC 6951 is inflowing or outflowing. Some models, beyond the scope of this paper, are necessary to make further interpretation of the velocity field and to derive meaningful quantities such as net mass infall rate.

3.3.4. Velocity dispersion

Fig. 15 shows the intensity-weighted CO velocity dispersion along the line of sight, as derived from the second moment of the CO data cube, $\sigma_v = (\Sigma(v_i - \langle v \rangle)^2 S_i) / (\Sigma S_i)$. This map shows the significant enhancement of the second moment value near the two CO peaks. The large velocity width near the CO peaks is also seen in the CO profile maps, Fig. 3(c). The southern CO peak is much weaker than the northern CO peak, but also shows a broad (FWZI ~ 200 km s $^{-1}$) line profile. Kenney (1996) also has pointed out that CO spectra near the northern CO peak show broad and complex line profiles in this galaxy. It should be noted, however, that this map contains both the intrinsic velocity dispersion of the gas and the gradient of rotation velocity in the observing beam. For instance, the very large velocity dispersion area along the minor axis of the galaxy seen in Fig. 15 represents the steep rise of the rotation curve in the central region of the galaxy. In order to estimate the intrinsic gas velocity dispersion σ_v , we subtracted the velocity component of the systematic velocity gradient within observing beam, σ_{rot} , from the observed velocity dispersion, σ_{obs} , as $\sigma_v = \sqrt{(\sigma_{\text{obs}})^2 - (\sigma_{\text{rot}})^2}$. A circular motion described by the rotation curve in Fig. 13 was assumed as a model velocity field in the subtraction. We find that gas the velocity dispersion is as high as ~ 50 km s $^{-1}$ in the Northern CO peak, and ~ 30 km s $^{-1}$ in the Southern CO peak. On the other hand, the velocity dispersion at the ring is in the range of 10 - 20 km s $^{-1}$. Note that these values are still upper limits to the true gas velocity dispersions because we don't take into account the non-circular motions here. Nevertheless, it is likely that the gas velocity dispersions at the CO peaks is significantly higher than that in the circumnuclear ring because shocks associated with the crowding of gas stream lines could keep the gas in a rather turbulent state there. Therefore, we speculate that the velocity dispersion in the CO peaks may be significantly larger than that in the circumnuclear ring.

4. Discussion

The CO and HCN data presented in the previous section revealed that the distribution of HCN emission is different from that of CO, in other words, there exists a spatial variation of the molecular line ratio $R_{\text{HCN}/\text{CO}}$. In this section, we discuss about the relationship between the observed properties of molecular gas and activities, namely, the circumnuclear star formation and

Seyfert nucleus.

4.1. Dense Molecular Gas Associated with the Circumnuclear Star Forming Ring

As seen in the previous section, the distribution of dense molecular gas correlates very well with the massive star forming region in the center of NGC 6951, and the $R_{\text{HCN}/\text{CO}}$ ratio is also enhanced at the circumnuclear ring where vigorous star formation occurs. A spatial coincidence of the HCN cloud complex and nuclear massive star forming regions, and an enhancement of $R_{\text{HCN}/\text{CO}}$ there, have been found in the central regions of other star forming galaxies, as listed in the previous section. These spatial coincidence between dense molecular gas and massive star forming regions is consistent with the quantitative correlation between HCN emission and tracers of massive star formation (Solomon et al. 1992; Gao & Solomon 1996; Zhao et al. 1996; Paglione, Jackson, & Ishizuki 1997). Considering the fact that stars are formed in the *dense molecular cores* rather than the diffuse envelopes of the molecular clouds in the Milky Way (e.g. Lada 1992), these quantitative and spatial correlation seem to indicate that the presence of dense molecular gas in these a few hundred parsec scale in the central regions of galaxies could be a *cause* of massive star formation. Therefore, it is now essential to address the formation mechanism of dense molecular clouds in order to explain the varieties of star formation in the central regions of galaxies.

What kind of physical processes govern the spatial variation of $R_{\text{HCN}/\text{CO}}$, namely, the distribution of dense molecular gas in the circumnuclear region of NGC 6951? Several mechanisms have been proposed to explain dense molecular gas cloud formation in the circumnuclear rings within the ILRs. One is the shocks along the orbit crowding; a crowding of gas stream lines will cause frequent collisions of the molecular gas clouds and shocks there, which can eventually form dense molecular gas (Combes & Gerin 1985). Another scenario is the gravitational instability of the accumulated gas near the ILRs (Elmegreen 1994). In order to address this issue, we first compared the distribution of $R_{\text{HCN}/\text{CO}}$ with the maps of the total gas surface density and the gas velocity dispersion, as shown in Fig. 16. In this comparison, we see the following two features, (i) in spite of the significant CO concentration, $R_{\text{HCN}/\text{CO}}$ is *not* enhanced in the crowding regions of $x1/x2$ orbits, and (ii) there exists a possible anti-correlation between $R_{\text{HCN}/\text{CO}}$ and the gas velocity dispersion. Any scenarios to explain dense molecular gas formation should also account for these observed features. In the following section, we will discuss about the several possible scenarios.

4.1.1. Shocks along the orbit crowding

It appears to be evident that a dense cloud formation scenario by shocks along the orbit crowding can not explain the observed feature (i). Dust lanes and the molecular gas spirals located at the leading edges of stellar bars are considered to trace shocks associated with the orbit

crowding of the distinct gas orbit families, x_1 and x_2 (e.g. Athanassoula 1992). In the case of NGC 6951, we find a possible infalling motion along the bar, and an enhancement of the CO velocity dispersion there, which may support the interpretations since these agree well with the theoretical predictions. We therefore conclude that the shocked regions along the leading edges of the bar does not promote the formation of *dense* molecular gas efficiently but enhance the presence of low density GMCs.

Similar situations can be found in the central regions of other galaxies; in the center of IC 342, a ring-like structure with two offset ridges of molecular gas is observed in CO emission (Ishizuki et al. 1990), while HCN emission is detected only in the central ring-like region (Downes et al. 1992). The ring-like gas distribution and two offset gas ridges are due to ILRs with a stellar bar (Böker, Förster-Schreiber, & Genzel 1997 and references therein). High CO brightness temperature, large gas velocity dispersion, and deviations from circular motions observed in the offset CO ridges strongly suggest the presence of shocks there (Ishizuki et al. 1990), however, the $R_{\text{HCN}/\text{CO}}$ ratio is as small as ~ 0.05 compared with the central ring region where $R_{\text{HCN}/\text{CO}}$ values are enhanced to ~ 0.12 (Downes et al. 1992). This is also the case in another barred spiral galaxy NGC 1530 (Reynaud & Downes 1997). As pointed out by Downes et al. (1996) and Reynaud & Downes (1997), these shocks along the orbit crowding regions may be too turbulent to form dense molecular gas and the dense molecular gas fraction remains rather low there. This would account for the low star formation efficiencies (SFEs) of the molecular gas along the dust lanes in the bar because the dense molecular gas fraction is considered to correlate with the SFEs (Solomon et al. 1992).

4.1.2. Gravitational instability

Another possibility is gravitational instabilities of the molecular gas. Especially, the observed feature (ii), that is a possible anti-correlation between the distribution of $R_{\text{HCN}/\text{CO}}$ and the gas velocity dispersion, implies that the large velocity dispersion in the orbit crowding region prevents the molecular gas from collapsing into the dense molecular clumps through the gravitational instabilities of the gas.

In order to check whether gravitational theory can successfully explain the spatial variation of the $R_{\text{HCN}/\text{CO}}$ or not, we estimated the Toomre Q parameter (Toomre 1964) in the circumnuclear region of NGC 6951. The Toomre Q parameter characterizes the criteria for local stability in thin isothermal disks and is expressed as $Q = \Sigma_{\text{crit}}/\Sigma_{\text{gas}}$, where Σ_{gas} is the molecular gas surface density $\Sigma_{\text{H}_2+\text{He}}$, and Σ_{crit} is the critical surface density, given by

$$\Sigma_{\text{crit}} = \frac{\sigma_r \kappa}{\pi G}, \quad (4)$$

where σ_r is the velocity dispersion in the radial direction, and κ is the epicyclic frequency. If the gas surface density Σ_{gas} exceeds the critical surface density Σ_{crit} , then an uniform gas disk is unstable to form rings or clumps which can ultimately collapse into dense molecular gas fragments

and form stars. Here we assume an isotropic velocity dispersion, namely, the velocity dispersion in the radial direction σ_r is the same as the one-dimensional velocity dispersion σ_v . At the radius of the ring, $r = 4''$ or 470 pc, we find Σ_{crit} is

$$\Sigma_{\text{crit}} = 630 \times \left(\frac{\sigma_v}{15 \text{ km s}^{-1}} \right) \left(\frac{\kappa}{0.57 \text{ km s}^{-1} \text{ pc}^{-1}} \right) M_{\odot} \text{ pc}^{-2}, \quad (5)$$

and an azimuthally averaged gas surface density $\Sigma_{\text{gas}} \sim 1.0 \times 10^3 M_{\odot} \text{ pc}^{-2}$. Then we obtain the Q value of 0.6, indicating that the molecular gas in the ring is gravitationally unstable. Therefore dense molecular clouds could be formed via gravitational instability of the molecular gas in the circumnuclear star forming ring of NGC 6951. It is then quite interesting to evaluate Q values in the outer regions of the ring where less active star formation occurs despite of strong CO emission, but it appears to be no longer valid to apply the Toomre's Q stability analysis in these regions because the gas morphology is far from an axisymmetric disk and the deviations of the gas orbits from circular motion are also significant there. We speculate that the molecular gas in the CO peaks may not be gravitationally unstable, probably due to the very large velocity dispersion there.

Next, we evaluated the time scale of the gravitational instability. The growth rate of the gravitational instability can be estimated as the Jeans time scale (e.g. Larson 1987),

$$t_J = \frac{\sigma_v}{\pi G \Sigma_{\text{gas}}} \simeq 1.1 \times 10^6 \times \left(\frac{\sigma_v}{15 \text{ km s}^{-1}} \right) \left(\frac{\Sigma_{\text{gas}}}{1.0 \times 10^3 M_{\odot} \text{ pc}^{-2}} \right)^{-1} \text{ yrs}, \quad (6)$$

for the averaged σ_v and Σ_{gas} at the radius of the ring. The rotation velocity at this radius is $\sim 160 \text{ km s}^{-1}$ from Fig. 13, and the dynamical time scale at this radius $t_{\text{dyn}} \sim 1.8 \times 10^7$ yrs. The time scale of the instability t_J does not conflict with the observed offset between the CO and HCN peaks, which is $t_{\text{offset}} \sim 1/6 t_{\text{dyn}} = 3.1 \times 10^6$ yrs at the radius of the ring.

In consequence, the gravitational instability scenario could nominally explain the features (i) and (ii). We therefore suggest that *gravitational instabilities of molecular gas are responsible for the dense molecular gas formation and successive star formation in the circumnuclear region of NGC 6951*. This is sketched in Fig. 17; the molecular gas along the dust lanes and successive CO arms are too turbulent to form dense molecular clouds, although the largest CO concentrations appear there. Some of the molecular gas escaped from the x_1/x_2 shocked regions is driven into the x_2 orbits, and become unstable ($Q \leq 1$) because of the smaller velocity dispersion on the x_2 orbit ring⁶. The dense molecular cores are formed via gravitational instabilities. The instabilities grow at a time scale of $t_J \sim 1 \times 10^6$ yrs, which does not conflict with the observed offset between the CO peaks and HCN peaks, $t_{\text{offset}} \sim 3 \times 10^6$ yrs. Massive star formation then will occur in these dense molecular clouds, showing a good coincidence between HCN emission and 6 cm radio continuum (or H α) emission.

⁶We note that Peng et al. (1996) have proposed that intense star formation occurs mostly in clouds on the x_2 orbits in the central region of nuclear starburst galaxy NGC 253, which may be similar to the case in NGC 6951.

The degree of gravitational stabilities seems to rule the formation of dense molecular clouds and successive star formation in other galaxies; in the nuclear starburst galaxy NGC 3504, the molecular gas is gravitationally unstable over the rigid rotating part of the rotation curve, where the starburst occurs (Kenney, Carlstrom, & Young 1993), and the dense molecular gas is concentrated in the same region as the starburst (Kohno et al. 1997). On the other hand, the molecular gas in the central a few hundred parsec region of NGC 4736 is found to be gravitationally *stable* (Shioya et al. 1998; Sakamoto et al. 1998; Kohno 1998), and we have found a remarkable decrease of HCN emission toward the central region of this galaxy (Kohno et al. 1997), despite the fact that the CO emission is concentrated there (Sakamoto et al. 1998). These results suggest again the presence of a strong connection between the degree of gravitational stabilities of the gas and the dense molecular gas formation, as in the case of NGC 6951. Note that the nucleus of NGC 4736 is known as a “post-starburst” (Pritchett 1977; Rieke, Lebofsky, & Walker 1988; Walker, Lebofsky, Rieke 1988; Taniguchi et al. 1996), where its current star formation rate is significantly depressed. Therefore the observed $R_{\text{HCN/CO}}$ value of ≤ 0.04 (2σ upper limit) in the post-starburst region of NGC 4736 (Kohno et al. 1997), which is much lower than starbursts ($R_{\text{HCN/CO}} \sim 0.1 - 0.2$; see Section 3.2), also supports the existence of a tight connection between dense molecular gas and massive star formation (Solomon et al. 1992; Jackson et al. 1996; Paglione, Jackson, & Ishizuki 1997). There are other objects where the gravitational instabilities may govern the star formation, such as NGC 4102 (Jogee & Kenney 1996), NGC 4314 (Kenney 1997), NGC 4414 (Sakamoto 1996; Braine, Brouillet, & Baudry 1997) and NGC 7331 (Shioya & Tosaki 1997), although no HCN maps are available for these galaxies yet. In a much larger (\geq a few kpc) scale, Kennicutt (1989) has successfully explained the threshold gas surface density for the star formation in the disk of galaxies via gravitational instabilities of the gas.

Although Kennicutt (1989) assumed a constant gas velocity dispersion in his work, variation of gas velocity dispersion may be intimately related to the gravitational instability of the gas as pointed out by Sakamoto (1996). Contini et al. (1997) claimed that the older starbursts have larger CO velocity dispersion in a kilo-parsec scale. At the GMC scale, the GMCs which have larger velocity dispersion possess less active star formation (Ikuta & Sofue 1997). Perhaps these results also imply the importance of the gas velocity dispersion on star formations at various spatial scales from GMCs to kilo-parsec scale galactic disks.

4.2. Dense Molecular Gas toward the Seyfert Nucleus of NGC 6951

The $R_{\text{HCN/CO}}$ averaged over the central $r < 120$ pc region was 0.086 toward the Seyfert nucleus in NGC 6951 (Fig. 8). This $R_{\text{HCN/CO}}$ value is in contrast to NGC 1068 and M51, where very high $R_{\text{HCN/CO}}$ values of 0.5 were reported (Jackson et al. 1993; Tacconi et al. 1994; Helfer & Blitz 1995; Kohno et al. 1996; Matsushita et al. 1998). What makes the difference of $R_{\text{HCN/CO}}$ in these Seyfert nuclei?

A difference of CO and/or HCN fractional abundance may be a possible explanation because

the strong X-ray radiation from the active nucleus has been claimed to cause the extremely high $R_{\text{HCN}/\text{CO}}$ reported in NGC 1068 (Leep & Dalgarno 1996; Shalabiea & Greenberg 1996). Therefore it is useful to compare the X-ray luminosity in these Seyfert galaxies, however, the intrinsic X-ray luminosity is quite difficult to measure due to the heavy absorption along the line of the sight in these type-2 AGN even in hard X-ray band.

On the other hand, very high $R_{\text{HCN}/\text{CO}}$ can be explained without such abundance effect. Matsushita et al. (1998) found that the molecular gas toward the center of M51 is characterized by an extreme physical condition, that is, a high temperature ($T_{\text{kin}} \gtrsim 100$ K) and high density ($n_{\text{H}_2} \sim 10^{5\pm 1} \text{ cm}^{-3}$). It should be noted that this result does scarcely depend on the adopted fractional HCN abundance. Very high temperature and high density molecular gas has suggested even in the central region of NGC 1068 (Tacconi et al. 1994; Helfer & Blitz 1995). Meanwhile, the observed $R_{\text{HCN}/\text{CO}}$ of 0.086 in NGC 6951 is similar to the value in the central ~ 600 pc region of the Milky Way, 0.08 (Jackson et al. 1996; Helfer & Blitz 1997a) where considerable amount of low density ($n_{\text{H}_2} \sim 10^2 \text{ cm}^{-3}$) molecular gas exist as well as high density molecular gas (e.g. Oka et al. 1998). Therefore we conclude that the rather normal $R_{\text{HCN}/\text{CO}}$ in NGC 6951 may be attributed to the different physical condition of the molecular gas in NGC 6951 from those in NGC 1068 and M51.

We speculate that the difference of physical conditions of the molecular gas might be related to the existence of large scale (kpc scale) nuclear jets and ionized gas outflow; both NGC 1068 and M51 possess a kpc scale jet, whereas NGC 6951 does not. The projected length of radio jet in NGC 1068 and M51 is ~ 1.3 kpc (Wilson & Ulvestad 1987; Gallimore et al. 1996) and ~ 1 kpc (Ford et al. 1985; Crane & van der Hulst 1992), respectively. On the contrary, the central peak seen in a 20 cm radio continuum map (Vila et al. 1990) is not resolved in the $\sim 1''$ beam, imposing an upper limit of ~ 120 pc for the length of the radio jet if it exists ⁷. Although these lengths are projected ones, a large scale jet in a pole-on configuration can not be likely in NGC 6951 because this is a type-2 AGN. Therefore the presence of dense ($n_{\text{H}_2} \sim 10^5 \text{ cm}^{-3}$) molecular material toward the nucleus may be a result or cause of the nuclear jet/outflow. Indeed, an interaction between nuclear jet/outflow and molecular gas has been suggested in NGC 1068 in order to explain the beam filling factor of the HCN emission which is comparable with that of the CO (Tacconi et al. 1994). That would be also the case in M51; the line width of the HCN(1–0) emission toward the nucleus of M51 is wider than that of the CO(1–0) emission by a few tens km s^{-1} and this may also imply an interaction between dense molecular gas and the nuclear jet/outflow (Kohno et al. 1996). The asymmetric line profile from dense molecular gas is clearly seen even in the CO(2–1) emission (Scoville et al. 1998). Alternatively, these dense molecular gas plays a role for the confinement of the jet/outflow (e.g. Irwin & Seaquist 1988; Blietz et al. 1994; Gallimore et al. 1996; Scoville et al. 1998).

⁷The 6 cm radio continuum map in Fig. 5 (Saikia et al. 1994) shows a bridge like extension from the nucleus, however, this is the effect of the elongated beam size. In fact, an higher resolution 6 cm image clearly shows an unresolved nuclear source (Saikia, private communication)

5. Conclusions

We present high resolution ($3'' - 5''$) observations of CO(J=1–0) and HCN(J=1–0) emission from the circumnuclear star forming ring in the barred spiral galaxy NGC 6951, a host of a type-2 Seyfert nucleus, using the Nobeyama Millimeter Array and the Nobeyama 45 m telescope. The results of our new observations and conclusions drawn from them are summarized as follows:

1. We find that the distribution of the HCN emission is different from that of CO in the circumnuclear region of NGC 6951; it is confirmed that CO emission is dominated by a “twin peaks” morphology with two spiral arms, which are connected to the dust lanes, as reported by Kenney et al. (1992). On the other hand, although the HCN emission also shows a twin peaks morphology, the HCN peaks are spatially shifted downstream compared with the CO peaks.
2. Most of the HCN emission is associated with the circumnuclear ring, where vigorous star formation occurs. In other words, the HCN emission spatially correlates better with the massive star forming regions than that of CO emission in the circumnuclear region of NGC 6951.
3. The HCN to CO integrated intensity ratio in the brightness temperature scale, $R_{\text{HCN/CO}}$, is enhanced in the star forming ring. The peak value of the $R_{\text{HCN/CO}}$ is about 0.16 – 0.18, which is comparable to the $R_{\text{HCN/CO}}$ in the starburst regions of NGC 253 and M82.
4. The formation mechanism of dense molecular gas has been investigated. No significant enhancement of $R_{\text{HCN/CO}}$ is observed at the CO peaks, which are interpreted as x_1/x_2 orbit crowding regions. This suggests that the shocks along the orbit crowding do not promote the formation of the dense molecular gas effectively but enhance the presence of low density GMCs in NGC 6951. Instead, gravitational instability can account for the dense molecular gas formation in the circumnuclear star forming ring because Toomre’s Q value is below unity there.
5. $R_{\text{HCN/CO}}$ is 0.086 averaged over the central $r < 120$ pc region toward the nucleus of NGC 6951, which shows a type-2 Seyfert activity. This is a rather normal value compared with non-active galaxies such as the Milky Way, and quite different from other type-2 Seyfert galaxies NGC 1068 and M51 where extremely high $R_{\text{HCN/CO}}$ value, ~ 0.5 , are reported. The variety of $R_{\text{HCN/CO}}$ value in these Seyfert nuclei would be attributed with the different physical conditions of the molecular gas around the active nuclei. The presence of large scale nuclear jets/outflows might be related to these difference of molecular gas properties.

We would like to thank the referee, Dr. J. D. P. Kenney, for the critical reading of the manuscript and invaluable suggestions which greatly improved this work. We are grateful to Dr.

H. Wozniak and Dr. P. Martine for sending us their H α image of NGC 6951, Dr. A. J. Barth for his HST V-band image, and Dr. D. J. Saikia for providing us with his not yet published new radio continuum map. We thank S. Takakuwa for providing us with his LVG code. We thank T. Kamazaki for assistance with making the figures. We are deeply indebted to the NRO staff for the operation of the telescopes and the continuous efforts in improving the performance of the instruments. K. K. was financially supported by the Japan Society for the Promotion of Science.

REFERENCES

- Aalto, S. Booth, R. S., Black, J. H., & Johansson, L. E. B., 1995, *A&A*, 300, 369
- Athanassoula, E. 1992, *MNRAS*, 259, 345
- Barth, A. J., Ho, L. C., Filippenko, A. V., & Sargent W. L. W. 1995, *AJ*, 110, 1009
- Benedict, G. F., Smith, B. J., & Kenney, J. D. P. 1996, *AJ*, 111, 1861
- Böker, T., Förster-Schreiber, N. M., & Genzel, R. 1997, *AJ*, 114, 1883
- Blietz, M., Cameron, M., Drapatz, S., Genzel, R., Krabbe, A., & van der Werf, P. 1994, *ApJ*, 421, 92
- Boer, B., & Schulz, H. 1993, *A&A*, 227, 397
- Bottinelli, L., Gouguenheim, L., Paturel, G., & Devaucouleurs, G. 1984, *A&AS*, 56, 381
- Braine, J., Brouillet, N., & Baudry, A. 1997, *A&A*, 318, 19
- Brouillet, N., & Schilke, P. 1993, *A&A*, 277, 381
- Buta, R., & Crocker, D. A. 1993, *AJ*, 105, 1344
- Combes, F., & Gerin, M. 1985, *A&A*, 150, 327
- Contini, T., Wozniak, H., Considere, S., & Davoust, E. 1997, *A&A*, 318, 51
- Crane, P. C., & van der Hulst, J. M. 1992, *AJ*, 103, 1146
- de Vaucouleurs, G., de Vaucouleurs, A., Corwin, H. G., Buta, R. J., Paturel, G., & Fouque, P. 1991, *Third Reference Catalogue of Bright Galaxies* (New York: Springer-Verlag)
- Downes, D., Radford, S. J. E., Guilloteau, S., Guélin, M., Greve, A., & Morris, D. 1992, *A&A*, 262, 424
- Downes, D., Reynaud, D., Solomon, P. M., Radford, S. J. E. 1996, *ApJ*, 461, 186
- Elmegreen, B. G., 1994, *ApJ*, 425, L73
- Elmegreen, D. M., Elmegreen, B. G., Chromey, F. R., Hasselbacher, D. A., & Bissell, B. A. 1996, *AJ*, 111, 1880
- Ford, H. C., Crane, P. C., Jacoby, G. H., Lawrie, D. G. 1985, *ApJ*, 293, 132
- Friedli, D., Wozniak, H., Rieke, M., Martinet, L., & Bratschi, P. 1996, *A&AS*, 118, 461

- Gao, Y., & Solomon, P. M. 1996, in CO: Twenty-Five Years of Millimeter-Wave Spectroscopy, ed. Latter, W. B., Radford, S. J. E., Jewell, P. R., Mangum, J. G., & Bally, J., (Dordrecht: Kluwer), 419
- Gallimore, J. F., Baum, S. A., O’Dea, C. P., & Pedlar, A., 1996, *ApJ*, 464, 198
- Goldreich, P., & Kwan, J. 1974, *ApJ*, 189, 441
- Golla, G., Allen, M. L., & Kronberg, P. P. 1996, *ApJ*, 473, 244
- González-Delgado, R. M., Pérez, E., Tadhunter, C., Vilchez, J. M., & Rodríguez-Espinosa, J. M. 1997, *ApJS*, 108, 155
- Güsten, R., Serabyn, E., Kasemann, C., Schinckel, A., Schneider, G., Schulz, A., & Young, K. 1993, *ApJ*, 402, 537
- Henkel, C., Baan, W. A., & Mauersberger, R. 1991, *A&A Rev.*, 3, 47
- Helfer, T., & Blitz, L. 1993, *ApJ*, 419, 86
- Helfer, T., & Blitz, L. 1995, *ApJ*, 450, 90
- Helfer, T., & Blitz, L. 1997, *ApJ*, 478, 162
- Helfer, T., & Blitz, L. 1997, *ApJ*, 478, 233
- Ho, L. C., Filippenko, A. V., & Sargent, W. L. W. 1995, *ApJS*, 98, 477
- Ho, L. C., Filippenko, A. V., & Sargent, W. L. W. 1997, *ApJS*, 112, 315
- Irvine, W. M., Goldsmith, P. F., & Hjalmarsen, Å. 1987, in *Interstellar Processes*, ed. D. J. Hollenbach & H. A. Thronson, Jr. (Dordrecht: Reidel Publishing Company), 561
- Irwin, J. A., & Seaquist, E. R. 1988, *ApJ*, 335, 658
- Ishizuki, S., Kawabe, R., Ishiguro, M., Okumura, S. K., Morita, K. -I., Chikada, Y., Kasuga, T. 1990, *Nature*, 344, 224
- Ikuta, C., & Sofue, Y. 1997, *PASJ*, 49, 323
- Jackson, J. M., Paglione, T. D., Ishizuki, S., & Rieu, N. Q. 1993, *ApJ*, 418, L13
- Jackson, J. M., Heyer, M. H., Paglione, T. A. D., & Bolatto, A. D. 1996, *ApJ*, 456, L91
- Jogee, S., & Kenney, J. D. P. 1996, in *Barred Galaxies*, ed. R. Buta, D. A. Crocker, & B. G. Elmegreen (San Francisco: ASP), 230
- Kenney, J. D. P., Wilson, C. D., Scoville, N. Z., Devereux, N. A., & Young, J. Y. 1992, *ApJ*, 395, L79

- Kenney, J. D. P., Carlstrom, J. E., & Young, J. S. 1993, *ApJ*, 418, 687
- Kenney, J. D. P. 1996, in *Barred Galaxies*, ed. R. Buta, D. A. Crocker, & B. G. Elmegreen (San Francisco: ASP), 150
- Kenney, J. D. P. 1997, in *Starburst Activity in Galaxies*, ed. J. Franco, R. Terlevich, & A. Serrano (Mexico: Rev. Mex. Astron. Ap), 52
- Kennicutt, R., C. 1983, *ApJ*, 272, 54
- Kennicutt, R., C. 1989, *ApJ*, 344, 685
- Kohno, K., Kawabe, R., Tosaki, T., & Okumura, S. K. 1996, *ApJ*, 461, L29
- Kohno, K., Kawabe, R., Sakamoto, K., Ishizuki, S., & Vila-Vilaró, B. 1997, in *The Central Regions of Galaxy and Galaxies*, ed. Y. Sofue (Dordrecht: Kluwer), in press
- Kohno, K. 1998, Ph.D Thesis, University of Tokyo
- Kuno, N., Nakai, N., Nishiyama, K., Sorai, K., Handa, T., & Iga, T. 1997, in *The Central Regions of Galaxy and Galaxies*, ed. Y. Sofue (Dordrecht: Kluwer), in press
- Lada, E. 1992, *ApJ*, 393, L25
- Larson, R. B. 1987, in *Starburst and Galaxy Evolution*, ed. T. X. Thuan, T. Montmerle, & J. Tran Thanh Van (Gif-sur-Yvette: Editions Frontieres), 467
- Leep, S., & Dalgarno, A. 1996, *A&A*, 306, L21
- Márquez, I., & Moles M. 1993, *AJ*, 105, 2090
- Matsushita, S., Kohno, K., Vila-Vilaró, B., Tosaki, T., & Kawabe, R. 1998, *ApJ*, 495, 267
- Mauersberger, R., & Henkel, C. 1989, *A&A*, 223, 79
- Mulchaey, J. S., Regan, M. W., & Kundu, A. 1997, *ApJS*, 110, 229
- Nguyen-Q-Rieu, Jackson, J. M., Henkel, C., Truong-Bach, & Mauersberger, R. 1992, *ApJ*, 399, 521
- Oka, T., Hasegawa, T., Hayashi, M., Handa, T., Sakamoto, S., 1998, *ApJ*, 493, 730
- Paglione, T. A. D., Jackson, J. M., Ishizuki, S., & Nguyen-Q-Rieu, 1995, *AJ*, 109, 1716
- Paglione, T. A. D., Tosaki, T., & Jackson, J. M. 1995, *ApJ*, 454, L117
- Paglione, T. A. D., Jackson, J. M., & Ishizuki, S. 1997, *ApJ*, 484, 656
- Paglione, T. A. D., Jackson, J. M., Bolatto, A. D., & Heyer, M. H. 1998, *ApJ*, 493, 680

- Peng, R., Zhou, S., Whiteoak, J. B., Lo, K. Y., & Sutton, E. C. 1996, *ApJ*, 470, 821
- Pritchett, C. 1977, *ApJS*, 35, 397
- Rieke, G. H., Lebofsky, M. J., & Walker, C. E. 1988, *ApJ*, 325, 679
- Reynaud, D., & Downes, D. 1997, *A&A*, 319, 737
- Robert, W. W., Huntley, J. M., & van Albada, G. D. 1979, *ApJ*, 233, 67
- Rozas, M., Beckman, J. E., & Knapen, J. H. 1996, *A&A*, 307, 735
- Sage, L. J., Shore, S. N., & Solomon, P. M. 1990, *ApJ*, 351, 422
- Saikia, D. J., Pedlar, A., Unger, S. W., & Axon, D. J. 1994, *MNRAS*, 270, 46
- Sakamoto, K., Okumura, S. K., Minezaki, T., Kobayashi, Y., & Wada, K. 1995, *AJ*, 110, 2075
- Sakamoto, K. 1996, *ApJ*, 471, 173
- Sakamoto, K., Okumura, S. K., Ishizuki, S., & Scoville, N. Z. 1998, *ApJ*, submitted.
- Sakamoto, S. 1997, *ApJS*, submitted.
- Sandage, A., & Tammann, G. 1981, *A Revised Sharpley-Ames Catalog of Bright Galaxies*
(Washington, DC: Carnegie Institution of Washington)
- Scoville, N. Z., Yun, M. S., Clemens, D. P., Sanders, D. B., & Waller, W. H. 1987, *ApJS*, 63, 821
- Scoville, N. Z., Yun, M. S., Armus, L., & Ford, H. 1998, *ApJ*, 493, L63
- Shalabiea, O. M., & Greenberg, J. M. 1996, *A&A*, 307, 52
- Shen, J., & Lo, K. Y. 1995, *ApJ*, 334, L99
- Shioya, Y., & Tosaki, T. 1997, *ApJ*, 484, 664
- Shioya, Y., Tosaki, T., Ohyama, Y., Murayama, T., Yamada, T., Ishizuki, S., & Taniguchi, Y.
1998, *PASJ*, 50, 317
- Solomon, P. M., & Scoville, N. Z. 1974, *ApJ*, 187, L71
- Solomon, P. M., Rivilo, A. R., Barrett, J., and Yahil, A. 1987, *ApJ*, 319, 730
- Solomon, P. M., Downes, D., & Radford, S. J. E. 1992, *ApJ*, 387, L55
- Tacconi, L. J., Genzel, R., Blietz, M., Cameron, M., Harris, A. I., & Madden, S. 1994, *ApJ*, 426,
L77
- Taniguchi, Y., Ohyama, Y., Yamada, T., Mouri, H., & Yoshida, M. 1996, *ApJ*, 467, 215

- Telesco, C. M., Dressel, L. L., & Wolstencroft, R. D. 1993, *ApJ*, 414, 120
- Toomre, A. 1964, *ApJ*, 139, 1217
- Tully, R. 1988, *Nearby Galaxies Catalog* (Cambridge: Cambridge Univ. Press)
- Turner, J. L., & Ho, P. T. P. 1983, *ApJ*, 268, L79
- Turner, J. L. 1994, in *Mass-Transfer Induced Activity in Galaxies*, ed. I. Shlosman (Cambridge: Cambridge Univ. Press), 91
- Vila M. B., Pedlar, A., Davies, R. D., Hummel, E., & Axon, D. J. 1990, *MNRAS*, 242, 379
- Walker, C. E., Lebofsky, M. J., & Rieke, G. H. 1988, *ApJ*, 325, 687
- Wilson, A. S., & Ulvestad J. S. 1987, *ApJ*, 319, 105
- Wozniak, H., Friedli, D., Martinet, L., Martin, P., & Bratschi, P. 1995, *A&AS*, 111, 115
- Wright, M. C. H., Ishizuki, S., Turner, J. L., Ho, P. T. P., & Lo, K. Y. 1993, *ApJ*, 406, 470
- Young, J. S., Xie, S., Tacconi, L., Knezek, P., Viscuso, P., Tacconi-Garman, L., Scoville, N., et al., 1995, *ApJS*, 98, 219
- Zhao, J. H., Anantharamaiah, K. R., Goss, W. M., & Viallefond, F. 1996, *ApJ*, 472, 54

Fig. 1.— An optical image from the Digitized Sky Survey and H α + N[II] contour map (white contours; Wozniak et al. 1995) in the central 3' \times 3' (21 kpc \times 21 kpc at $D = 24.1$ Mpc) field of NGC 6951. Contour levels of the H α + N[II] image are 1.0, 2.5, 5.0, 10.0, 15.0, 20.0, and 30.0 $\times 10^{-15}$ erg s $^{-1}$ cm $^{-2}$ arcsec $^{-2}$. The boundary of the H α + N[II] map is indicated by white lines. The mapped area with the NMA is also denoted as white dashed circles; the smaller and larger circles represent the NMA primary beam size at CO(1–0) observations (65'' HPBW) and HCN(1–0) observations (84''), respectively. It is evident that most of the star formation is confined within the circumnuclear ring.

Fig. 2.— Velocity channel maps of CO(1–0) and HCN(1–0) emission in the central 30'' \times 30'' (3.5 kpc \times 3.5 kpc at $D = 24.1$ Mpc) region of NGC 6951. The cross shows the position of the nucleus defined as the central peak of 6 cm radio continuum (Saikia et al. 1994). The attenuation due to the primary beam pattern is not corrected in these maps. (a) Channel maps of CO emission. The velocity width of each channels is 9.79 km s $^{-1}$ and the central velocities (V_{LSR} in km s $^{-1}$) are labeled. The beam size is 3''.9 \times 3''.1 with $P.A.$ of 0°. Contour levels are -4, -2, 2, \dots , 10, and 12 σ , where 1 $\sigma = 34$ mJy beam $^{-1}$ or 260 mK in T_b . Negative contours are dashed. (b) Channel maps of HCN emission. Velocity width of each channel is 38.2 km s $^{-1}$ and the central velocities (V_{LSR} in km s $^{-1}$) are labeled. The beam size is 4''.7 \times 4''.5, $P.A.$ 165°. Contour levels are -3, -1.5, 1.5, 3, 4.5, and 6 σ , where 1 $\sigma = 5.1$ mJy beam $^{-1}$ or 37 mK in T_b .

Fig. 3.— Integrated intensity maps and line profile maps of the CO(1–0) and HCN(1–0) emission, derived from the NMA data cubes, in the central 20'' \times 25'' (2.3 kpc \times 2.9 kpc) region of NGC 6951. The line profiles were measured at 5 \times 7 points on the 3'' spacing $\alpha - \delta$ grid. The grid positions are indicated by crosses in the integrated intensity maps. The central grid position corresponds to the nucleus defined as the 6 cm radio continuum peak (Saikia et al. 1994). The attenuation due to the primary beam pattern is corrected in these maps. (a) Integrated intensity map of CO(1–0) emission over a velocity range from $V_{\text{LSR}} = 1223$ to 1564 km s $^{-1}$. The beam size is 3''.9 \times 3''.1 with $P.A.$ of 0°. The contour levels of the CO map are 2, 4, 6, \dots , and 26 σ where 1 σ is 1.9 Jy beam $^{-1}$ km s $^{-1}$ or 15 K km s $^{-1}$, corresponding to a face-on molecular gas surface density $\Sigma_{\text{gas}} = 1.36 \times \Sigma_{\text{H}_2} = 73 M_{\odot} \text{pc}^{-2}$. (b) Integrated intensity map of HCN(1–0) emission over a velocity range from $V_{\text{LSR}} = 1225$ to 1567 km s $^{-1}$. The beam size is 4''.7 \times 4''.5, $P.A.$ 165°. The contour levels are 2, 3, 4, \dots , and 9 σ , where 1 $\sigma = 0.58$ Jy beam $^{-1}$ km s $^{-1}$ or 4.3 K km s $^{-1}$. (c) CO line profiles. The noise level is 34 mJy beam $^{-1}$ or 260 mK in T_b at the central position. The peak brightness temperature is ~ 3.5 K. The width of a velocity bin is 9.79 km s $^{-1}$. (d) HCN line profiles. The noise level is 5.1 mJy beam $^{-1}$ or 38 mK in T_b at the central position. The peak brightness temperature is ~ 0.38 K. The width of a velocity bin is 19.1 km s $^{-1}$.

Fig. 4.— CO(1–0) and HCN(1–0) spectra toward the nucleus of NGC 6951 taken with the NRO 45 m telescope (dashed line), together with spectra from the NMA observations (solid line). The velocity resolution of the CO spectrum is 10 km s $^{-1}$ and HCN is 20 km s $^{-1}$ for the 45 m spectra. Beam size (HPBW) at the frequencies of CO(1–0) and HCN(1–0) are 15'' and 19'', respectively.

The spectra from the NMA data are made after convolving the data cube to the same beam size as the 45 m beam.

Fig. 5.— Comparison of the CO(1–0) and HCN(1–0) distributions (thin contours) with the H α + [NII] (greyscale, Wozniak et al. 1995) and 6 cm radio continuum images (thick contours, Saikia et al. 1994). The seeing size of the H α + [NII] is about 1".5. The greyscale ranges from 1.30×10^{-15} to 3.07×10^{-14} ergs s $^{-1}$ cm $^{-2}$ arcsec $^{-2}$. The beam size of 6 cm radio map is $2''.57 \times 1''.44$ with a *P.A.* of 80°, and contour levels are 3, 6, 9, \dots , and 18 σ , where 1 σ = 60 μ Jy beam $^{-1}$. The traces of dust lanes seen in a *B* – *I* color image (Wozniak et al. 1995) are denoted as dashed lines. The ellipses show the synthesized beams of CO and HCN observations. The direction of the galactic rotation is indicated by an arrow. It is evident that the distribution of HCN emission is different from that of CO; the HCN peaks are spatially shifted downstream with respect to the CO peaks, and the most of HCN emission are associated with the circumnuclear star forming ring traced by H α and radio continuum emission.

Fig. 6.— Curves of constant $R_{\text{HCN/CO}}$ (solid lines) and brightness temperature of the HCN(1–0) emission (dashed lines) as functions of kinetic temperature and density of molecular gas. CO fractional abundance per unit velocity gradient $Z(\text{CO})/(dv/dr)$ was set to 10^{-4} , where $Z(\text{CO})$ is defined as $[\text{CO}]/[\text{H}_2]$, and the unit of dv/dr is km s $^{-1}$ pc $^{-1}$. The fractional abundance ratio of HCN and CO molecules were assumed to be $Z(\text{HCN})/Z(\text{CO}) = 1/4000$ (Irvine, Goldsmith, & Hjalmarson 1987).

Fig. 7.— (a) Map of the HCN(1–0)/CO(1–0) integrated intensity ratio in brightness temperature scale, $R_{\text{HCN/CO}}$. Contour levels are 0.08, 0.1, 0.12, \dots , and 0.18. Greyscale ranges from 0.08 to 0.2. The traces of dust lanes seen in a *B* – *I* color image (Wozniak et al. 1995) are denoted as dashed lines. (b) 6 cm radio continuum map (Saikia et al. 1994) superposed on the greyscale image of the $R_{\text{HCN/CO}}$ distribution. It is clear that the $R_{\text{HCN/CO}}$ is enhanced at the massive star forming regions traced by the radio continuum emission.

Fig. 8.— Radial profile of the $R_{\text{HCN/CO}}$ in the central region of NGC 6951. The ratio was averaged over the successive annuli with $1'' = 117$ pc width. The location of the circumnuclear star forming ring traced by H α emission is also indicated.

Fig. 9.— Definition of the polar coordinate for Fig. 10. $\phi = 0^\circ$ corresponds to the major axis of the galaxy.

Fig. 10.— CO, HCN, and $R_{\text{HCN/CO}}$ distributions on *R* – ϕ coordinate denoted as Fig. 9. Contour levels of CO and HCN maps are same as Fig. 3. Contour levels of $R_{\text{HCN/CO}}$ are 0.1, 0.12, 0.14, 0.16, and 0.18. The peak positions of CO and $R_{\text{HCN/CO}}$ are indicated as dashed lines. We see the spatial offset of HCN peaks with respect to the CO peaks, which is also evident in $R_{\text{HCN/CO}}$ map. The coincidence of the dense molecular gas and massive star forming regions traced by the 6 cm radio continuum is also clearly shown.

Fig. 11.— Intensity-weighted mean velocity map of the CO emission in the central region of NGC 6951, superposed on the grey-scale image of the velocity integrated intensity map of the CO emission. The contour interval is 20 km s^{-1} , and contours are labeled by the value of V_{LSR} . The contour which represents the systemic velocity, 1428 km s^{-1} , is displayed by a thick contour. Note that the “S-shape” contours near the systemic velocity, indicating the presence of non-circular motions there.

Fig. 12.— Position - velocity map (pv map) of the CO emission in NGC 6951 along the major axis ($P.A. = 130^\circ$). Contour levels are $-3, -1.5, 1.5, \dots, \text{and } 12 \sigma$, where $1 \sigma = 34 \text{ mJy beam}^{-1}$ or $260 \text{ mK in } T_b$. Negative contours are dashed. The cross indicates the kinematical center ($\delta(\text{B1950}) = +65^\circ 55' 46''.0, V_{\text{sys}} = 1428 \text{ km s}^{-1}$).

Fig. 13.— (a) Circular rotation curve of NGC 6951 derived from the intensity-weighted mean velocity map of the CO emission. This is derived from the intensity-weighted mean velocity map of the CO emission within $\pm 5^\circ$ of the major axis. Inclination (42°) is corrected. (b) Angular velocities Ω , epicyclic frequency κ , and $\Omega - \kappa/2$ as a function of galactocentric radius, derived from the CO circular rotation curve (a). The κ is divided by 2 to facilitate comparison. The horizontal line (dashed line) indicates an estimation of the bar pattern speed, $50 \text{ km s}^{-1} \text{ kpc}^{-1}$. Horizontal arrows show the loci of the ring and CO arms.

Fig. 14.— CO velocity residuals produced by subtracting the rotation curve in Fig. 12(a) from the observed mean velocity field in Fig. 10. Residuals are superposed on the integrated CO intensity greyscale map. The velocity interval is 15 km s^{-1} . Dust lanes are indicated by straight dashed lines. The largest deviations are seen on the CO arms which are connected to the dust lanes.

Fig. 15.— Intensity-weighted velocity dispersion map of the CO emission. The contour interval is 10 km s^{-1} . This map is computed by calculating the second order moment of intensity at each point from the CO cube. Note that this map contains both the intrinsic velocity dispersion of gas and the gradient of rotation velocity within the observed beam.

Fig. 16.— Comparison of $R_{\text{HCN}/\text{CO}}$ ratio distribution (greyscale) with contour maps of (a) the integrated CO intensity, and (b) the 2nd moment map of the CO cube. The greyscale ranges from 0.13 to 0.18. Contour intervals of (a) and (b) are same as Fig. 3(a) and Fig. 15. It is evident that the $R_{\text{HCN}/\text{CO}}$ ratio is not enhanced at the CO arms, which is thought to be a shocked region associated with the x_1/x_2 orbit crowding. There also exist a possible anti-correlation between the $R_{\text{HCN}/\text{CO}}$ and the gas velocity dispersion.

Fig. 17.— Schematic view of the CO and HCN morphology, and the gas motion in the central region of NGC 6951. The molecular gas along the dust lanes and successive CO arms are too turbulent to form dense molecular clouds, although the largest CO concentrations appear there. Some of the molecular gas escaped from the x_1/x_2 shocked regions is driven into the x_2 orbits, and become unstable ($Q < 1$) because of the smaller velocity dispersion on the x_2 orbit ring, and dense molecular cores are formed via gravitational instabilities. Massive star formation then will occur

in these dense molecular cores, showing a good coincidence between HCN emission and 6 cm radio continuum (or $H\alpha$) emission.

Table 1. Properties of NGC 6951.

Parameter	Value	Ref.
Morphology	SAB(rs)bc	RC3
	SB/SBb(rs)I.3	RSA
Nuclear activity	Type 2 Seyfert	(1)
Position of nucleus		(2)
α (B1950)	20 ^h 36 ^m 36 ^s .59	
δ (B1950)	+65°55′46″.0	
$D_{25} \times d_{25}$	3′.9 × 3′.2	RC3
Position angle	130°	(3)
Inclination angle	42°	(4)
Adopted Distance	24.1 Mpc	(5)
Linear scale	117 pc arcsec ⁻¹	
$S_{60\mu\text{m}}$	13.21 ± 0.528 Jy	(6)
$S_{100\mu\text{m}}$	37.47 ± 1.498 Jy	(6)
$L_{\text{FIR}}^{\text{a}}$	1.6 × 10 ¹⁰ L_{\odot}	...
$L_{\text{H}\alpha}$ (ring) ^b	4.2 × 10 ⁴¹ ergs s ⁻¹	...
SFR (ring) ^c	3.8 M_{\odot} yrs ⁻¹	...

^a L_{FIR} was calculated as $3.75 \times 10^5 \times (D/\text{Mpc})^2 (2.58S_{60\mu\text{m}} + S_{100\mu\text{m}})$ in L_{\odot} .

^bMeasured from the central 13'' × 13'' aperture in an H α + [NII] image (Wozniak et al. 1995). Contributions from the central 3'' × 3'' aperture (Seyfert nucleus) was subtracted. Internal extinction was corrected assuming $A_{\text{v}} = 3.4$ mag (Barth et al. 1995). $EW(\text{H}\alpha + [\text{NII}]) = 1.33 \times EW(\text{H}\alpha)$ was adopted (Kennicutt 1983).

^cSFR was derived from $L_{\text{H}\alpha}/(1.12 \times 10^{41} \text{ ergs s}^{-1})$ in $M_{\odot} \text{ yrs}^{-1}$ (Kennicutt 1983).

References. — (1) Ho et al. 1995; (2) Saikia et al. 1994; (3) This work; (4) Márquez & Moles 1993; (5) Tully 1988; (6) Ho et al. 1997

Table 2. NMA observations and results.

Parameter	Value	
Observing date	Nov. 1995 - Feb. 1996	
Number of antennas	6	
Array configuration	AB, C, & D	
Phase center		
α (B1950)	20 ^h 36 ^m 36 ^s .59	
δ (B1950)	+65°55'46''0	
Visibility calibrator	3C418	
Band width	319.815680 MHz	
Line-specific parameters		
Line and transition	CO(J=1–0)	HCN(J=1–0)
Rest frequency	115.271204 GHz	88.6316024 ^a GHz
Observed frequency	114.725 GHz	88.210 GHz
Projected baseline	3.8 – 73 k λ	2.9 – 102 k λ
Field of view	65'' (7.6 kpc)	84'' (9.8 kpc)
Velocity coverage	836 km s ⁻¹	1088 km s ⁻¹
Velocity resolution	9.79 km s ⁻¹	38.2 km s ⁻¹
Synthesized beam	3''9 \times 3''1, <i>P.A.</i> 0° (460 \times 360 pc)	4''7 \times 4''5, <i>P.A.</i> 165° (550 \times 530 pc)
Equivalent T_b for 1 Jy beam ⁻¹	7.7 K	7.4 K
r.m.s. noise in channel map	34 mJy beam ⁻¹ = 260 mK in T_b	5.1 mJy beam ⁻¹ = 38 mK in T_b
NMA flux within F.O.V.	334 \pm 12 Jy km s ⁻¹	18.7 \pm 1.9 Jy km s ⁻¹
FCRAO flux	350 \pm 41 Jy km s ⁻¹	...
S(NMA)/S(FCRAO)	0.95	...
Luminosity L'	4.8 \times 10 ⁸ K km s ⁻¹ pc ²	4.5 \times 10 ⁷ K km s ⁻¹ pc ²
Luminosity ratio L_{FIR}/L'^b	38	390

^aweighted mean of three hyper-fine transitions

^b $L_{\text{FIR}}/L'_{\text{CO}}$ and $L_{\text{FIR}}/L'_{\text{HCN}}$, respectively. L_{FIR} is in Table 1.

Note. — The uncertainties of fluxes are statistical errors only.

Table 3. 45 m observations and results.

Parameter	CO(J=1–0)	HCN(J=1–0)
Beam size (HPBW)	15''	19''
Main beam efficiency η_{MB}	0.45 ± 0.03	0.50 ± 0.03
Peak Temperature T_{MB}	380 ± 21 mK	38 ± 4.7 mK
Velocity width (FWZI)	380.2 ± 10 km s ⁻¹	364.2 ± 20 km s ⁻¹
Integrated intensity $\int T_{\text{MB}}(v)dv$	71 ± 8.0 K km s ⁻¹	6.5 ± 1.7 K km s ⁻¹
45 m flux ^a	172 ± 19 Jy km s ⁻¹	15.0 ± 3.9 Jy km s ⁻¹
NMA flux in same beam ^b	197 Jy km s ⁻¹	14.1 Jy km s ⁻¹
S(NMA)/S(45m)	1.1	0.94
Luminosity L'	2.4×10^8 K km s ⁻¹ pc ²	3.6×10^7 K km s ⁻¹ pc ²

^aThe CO and HCN fluxes calculated from the integrated intensities. The point source sensitivities of 2.4 Jy K⁻¹ and 2.3 Jy K⁻¹ are assumed for CO and HCN observations, respectively.

^bThe CO and HCN fluxes measured from the convolved cubes as the same beam size of 45 m observations.

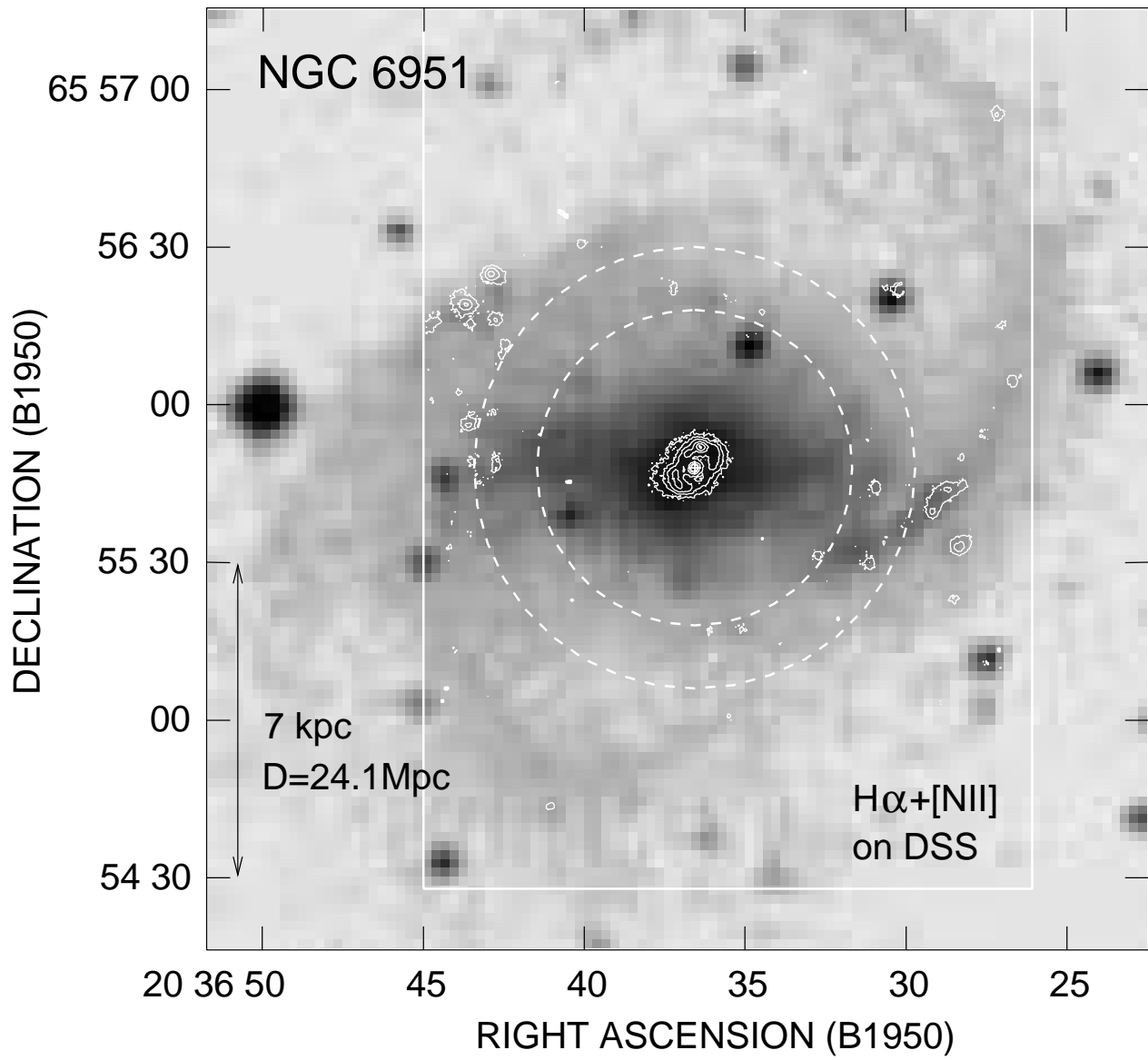
Note. — The uncertainties of fluxes are statistical errors only.

Table 4. Kinematical parameters derived from the CO velocity field^a

Parameter	Value
Kinematical center	
α (B1950)	$20^{\text{h}}36^{\text{m}}36^{\text{s}}.66 \pm 0^{\text{s}}.16$
δ (B1950)	$+65^{\circ}55'46''.3 \pm 1''$
Position angle	$130^{\circ} \pm 4^{\circ}$
Systemic velocity ^b	$1428 \text{ km s}^{-1} \pm 2 \text{ km s}^{-1}$

^afitting was made within the $1'' < r < 5''$ region.

^bLSR velocity. Subtract 14.4 km s^{-1} to obtain heliocentric velocities.



Kohno, Kawabe, and Vila-Vilaro 1998
Figure 1

This figure "figure2a.gif" is available in "gif" format from:

<http://arxiv.org/ps/astro-ph/9808229v1>

This figure "figure2b.gif" is available in "gif" format from:

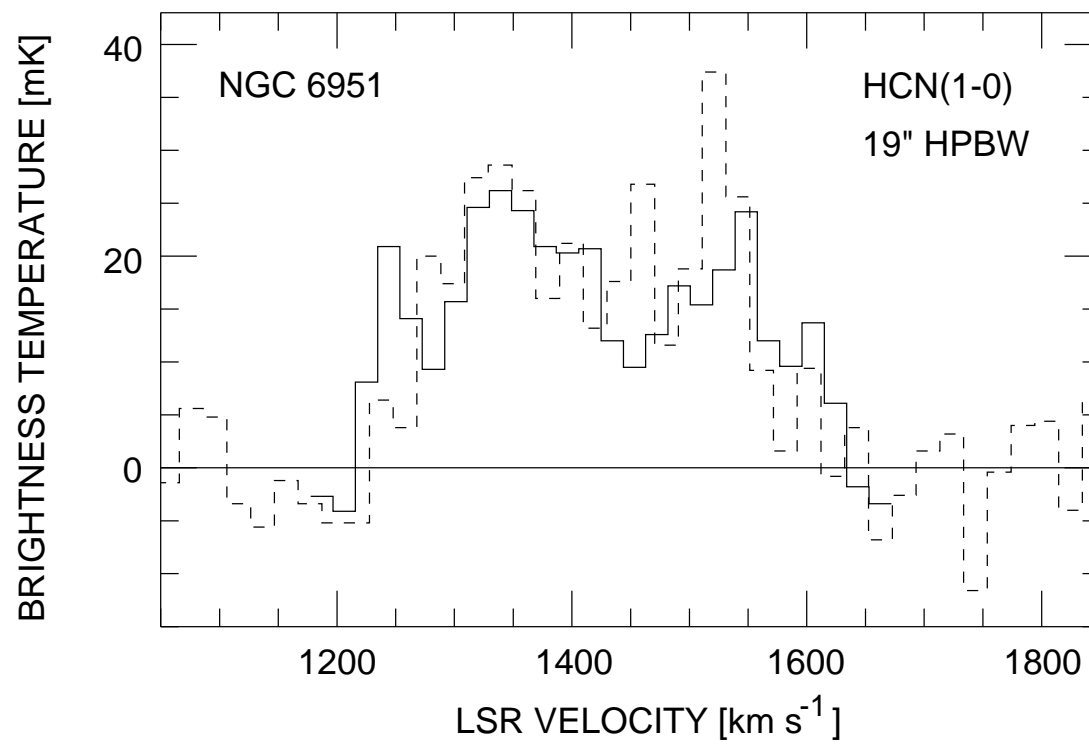
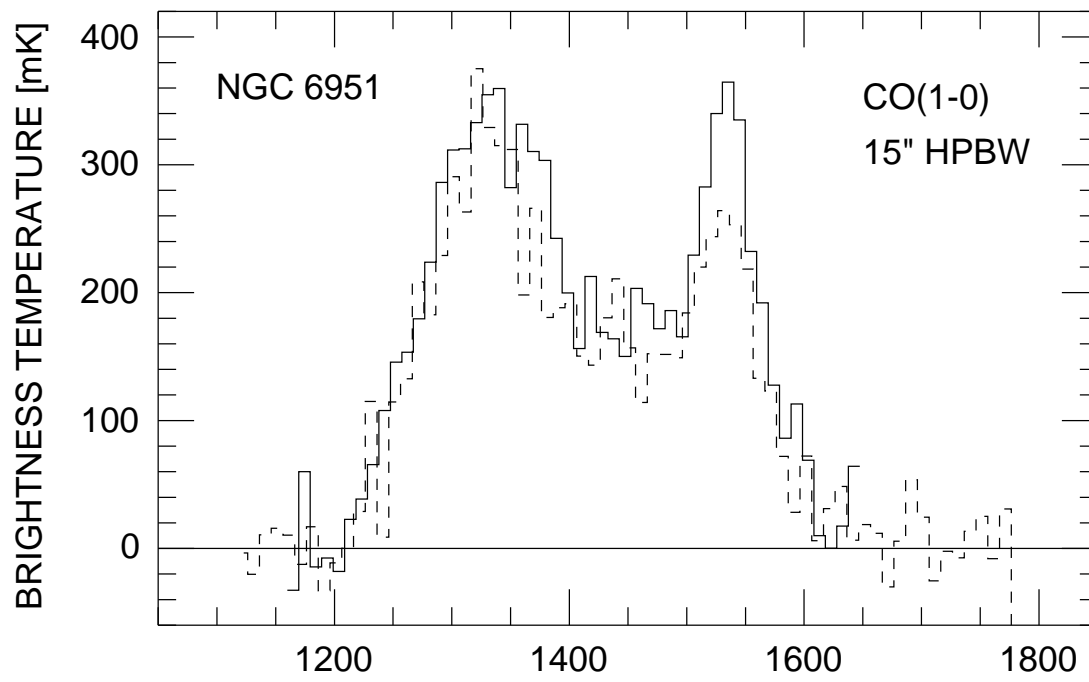
<http://arxiv.org/ps/astro-ph/9808229v1>

This figure "figure2c.gif" is available in "gif" format from:

<http://arxiv.org/ps/astro-ph/9808229v1>

This figure "figure3.gif" is available in "gif" format from:

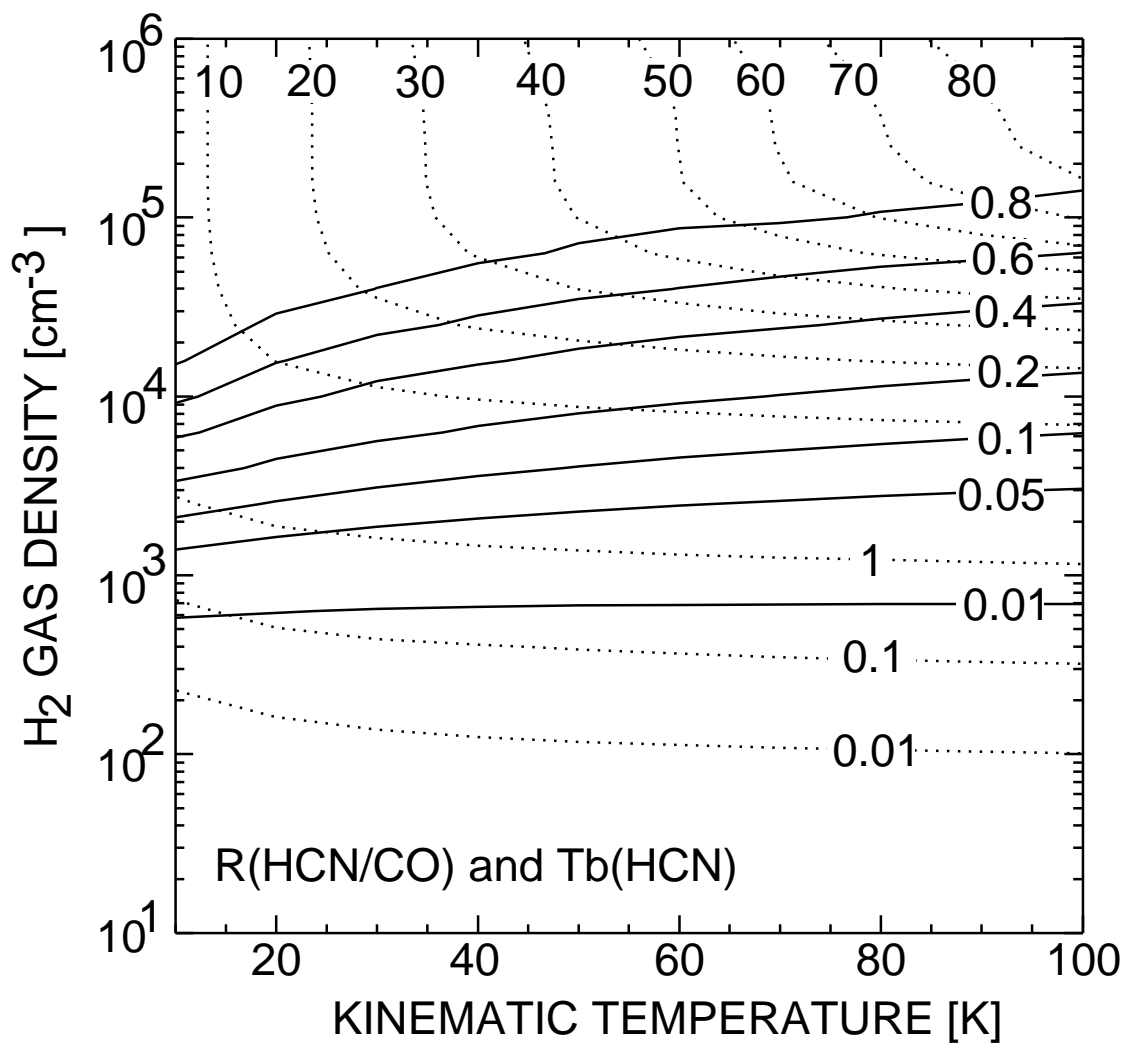
<http://arxiv.org/ps/astro-ph/9808229v1>



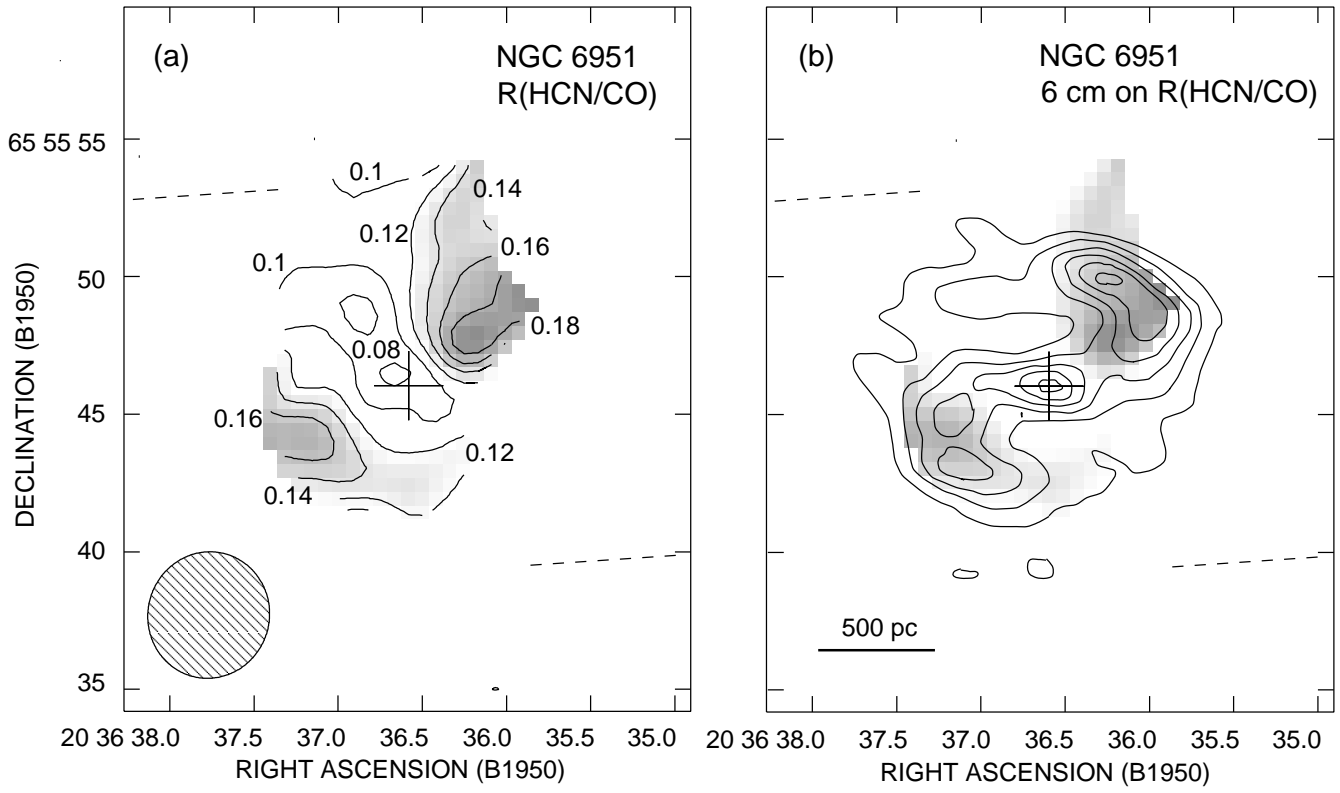
Kohno, Kawabe, and Vila-Vilaro 1998
Figure 4

This figure "figure5.gif" is available in "gif" format from:

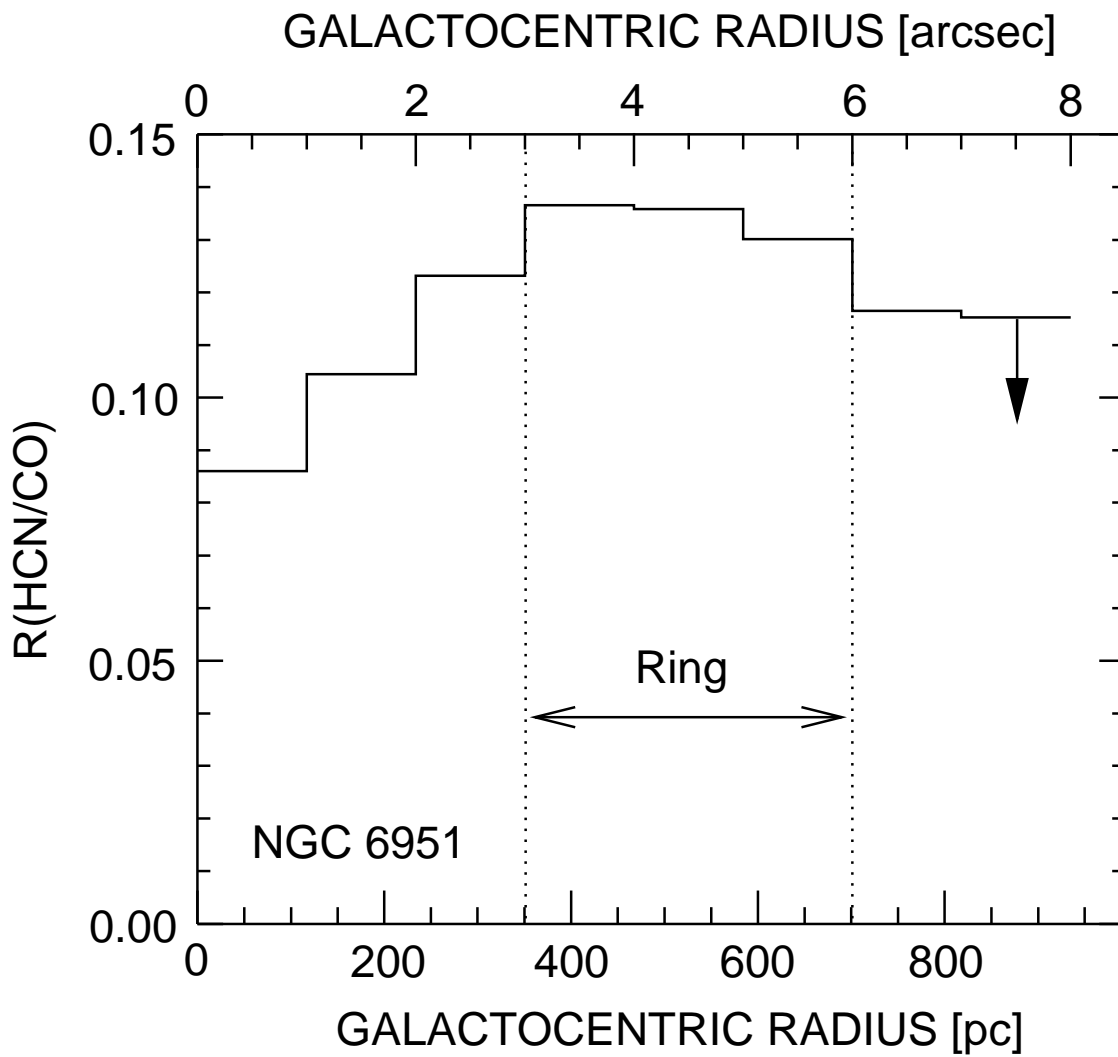
<http://arxiv.org/ps/astro-ph/9808229v1>



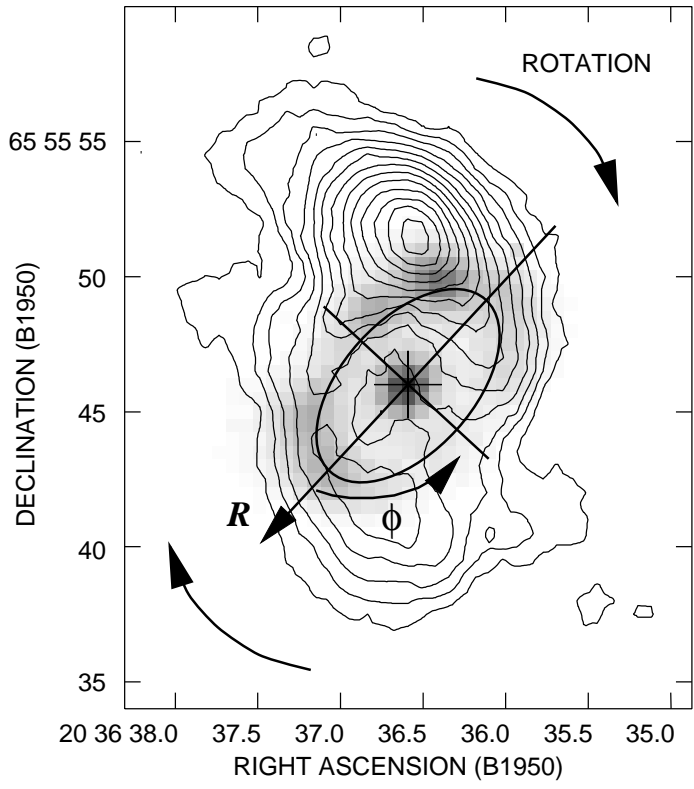
Kohno, Kawabe, and Vila-Vilaro 1998
Figure 6



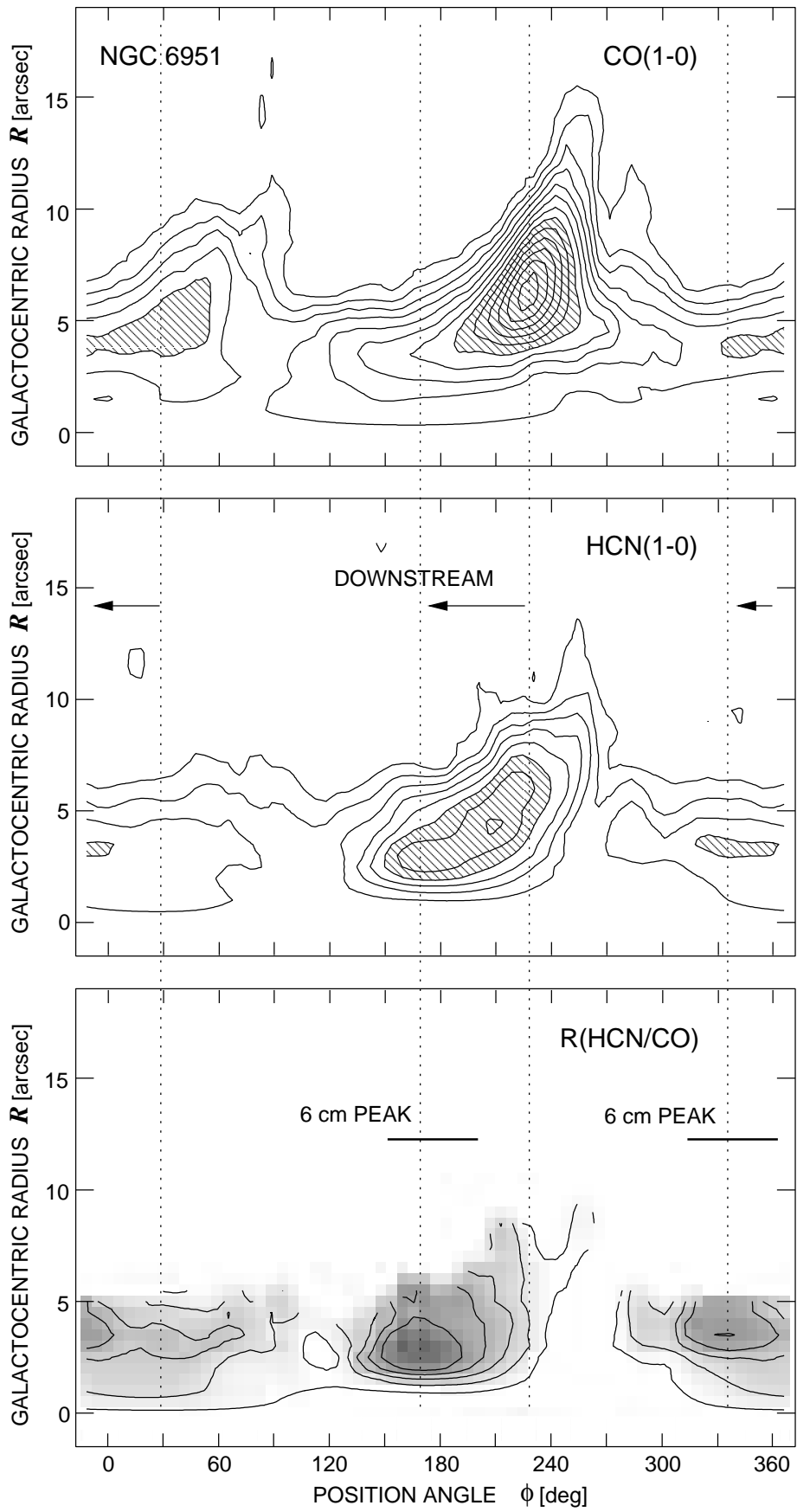
Kohno, Kawabe, and Vila-Vilaro 1998
Figure 7



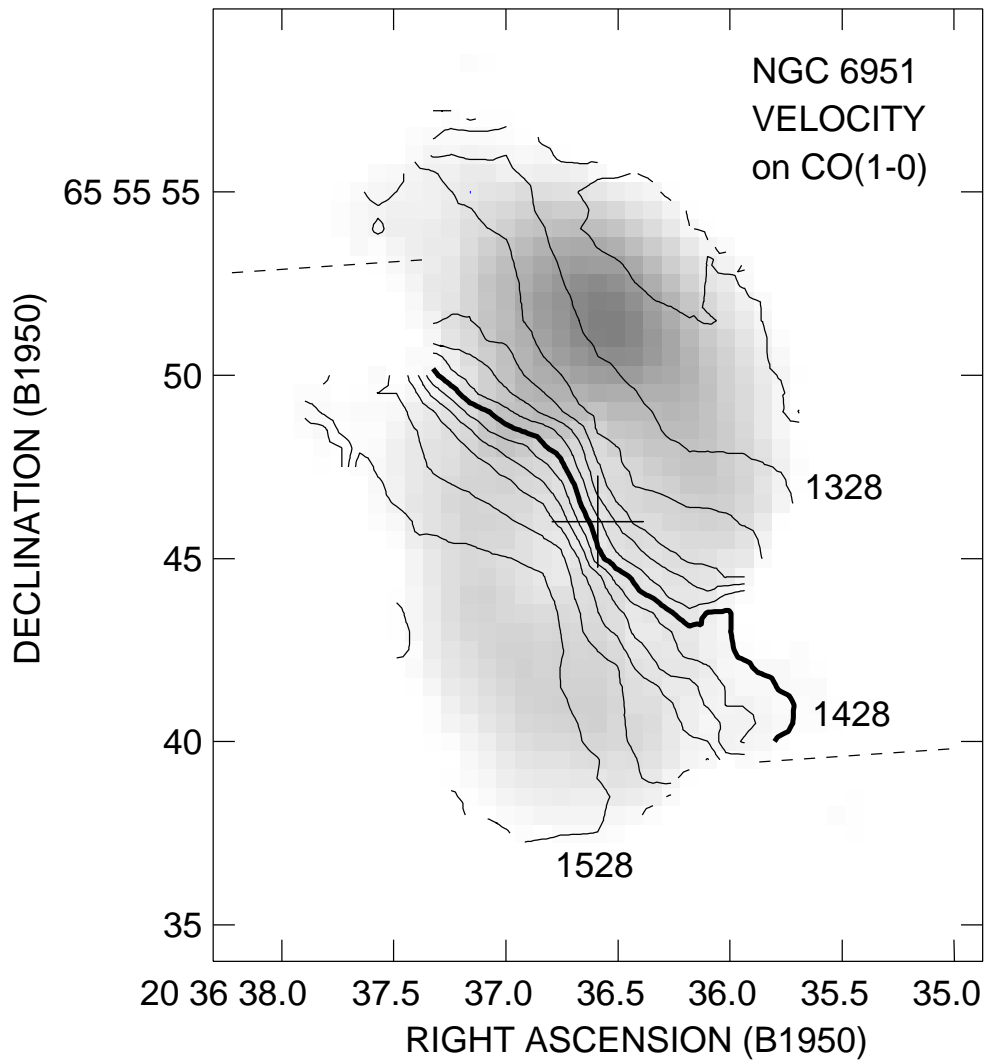
Kohno, Kawabe, and Vila-Vilaro 1998
Figure 8



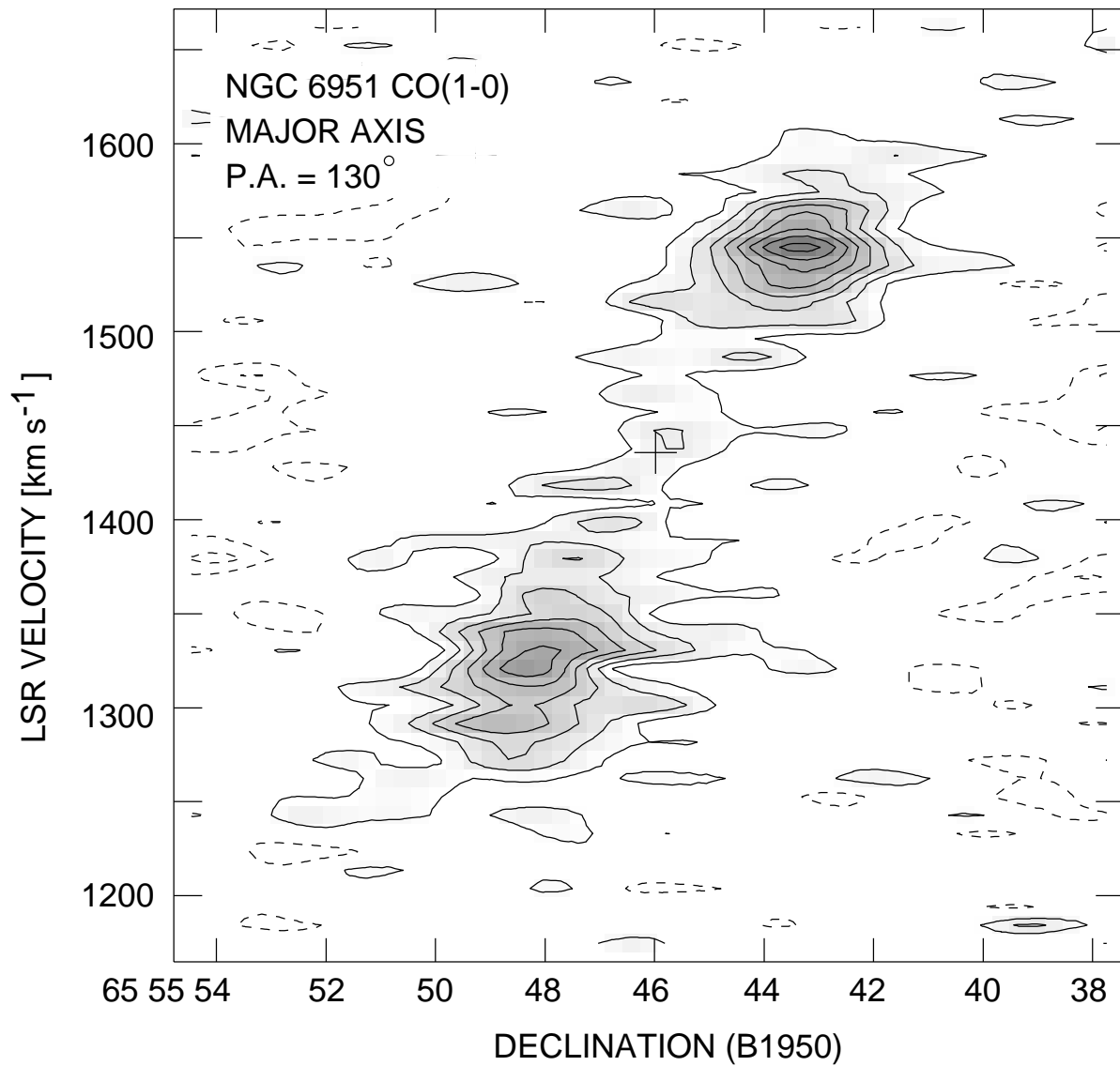
Kohno, Kawabe, and Vila-Vilaro 1998
Figure 9



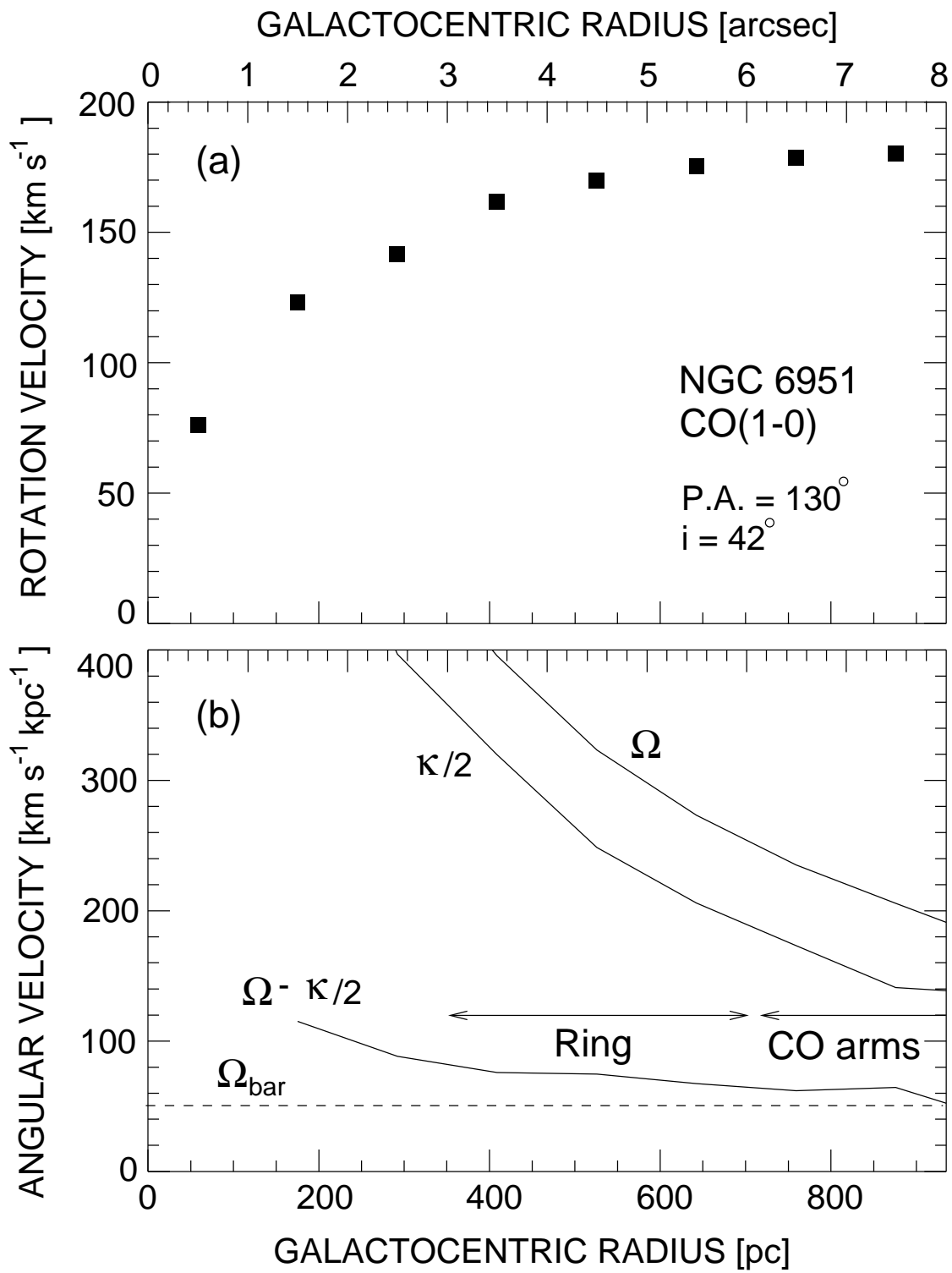
Kohno, Kawabe, and Vila-Vilaro 1998
Figure 10



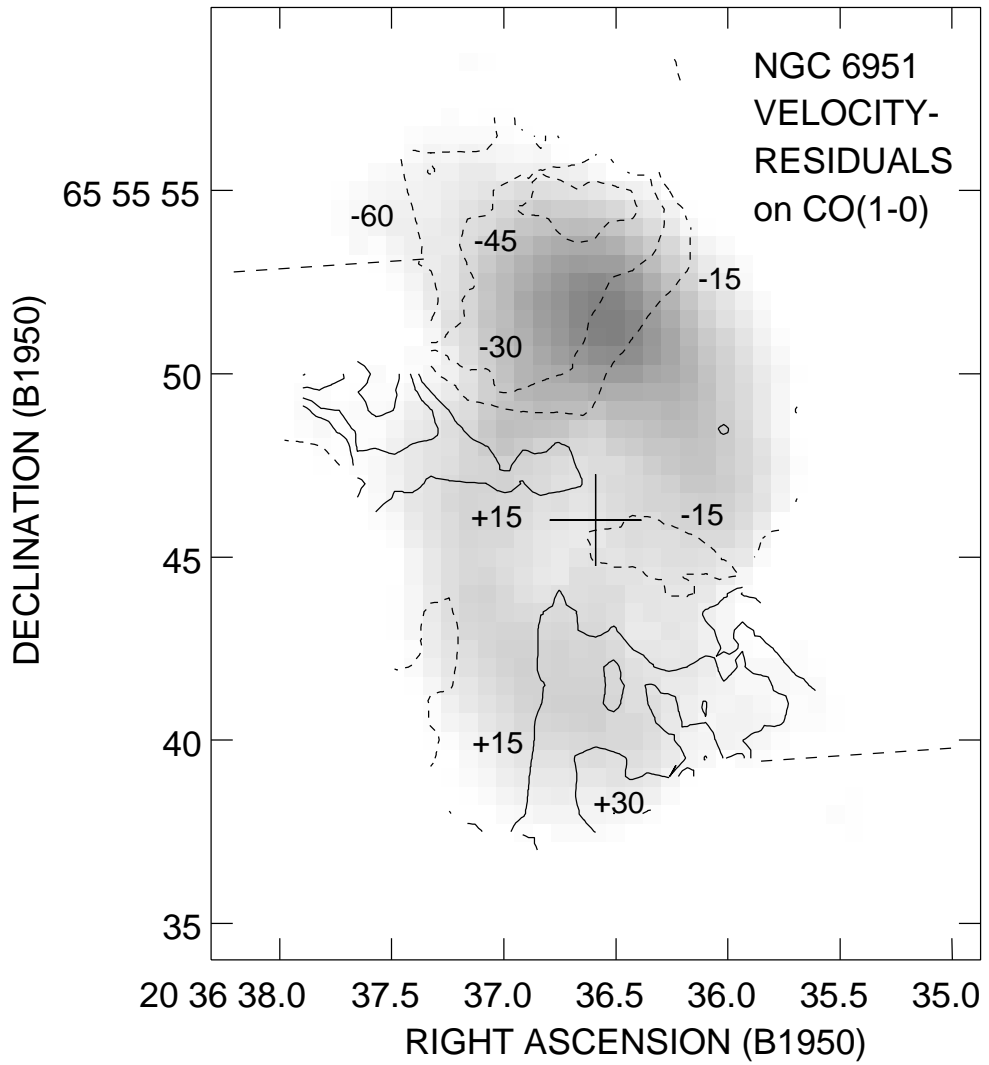
Kohno, Kawabe, and Vila-Vilaro 1998
Figure 11



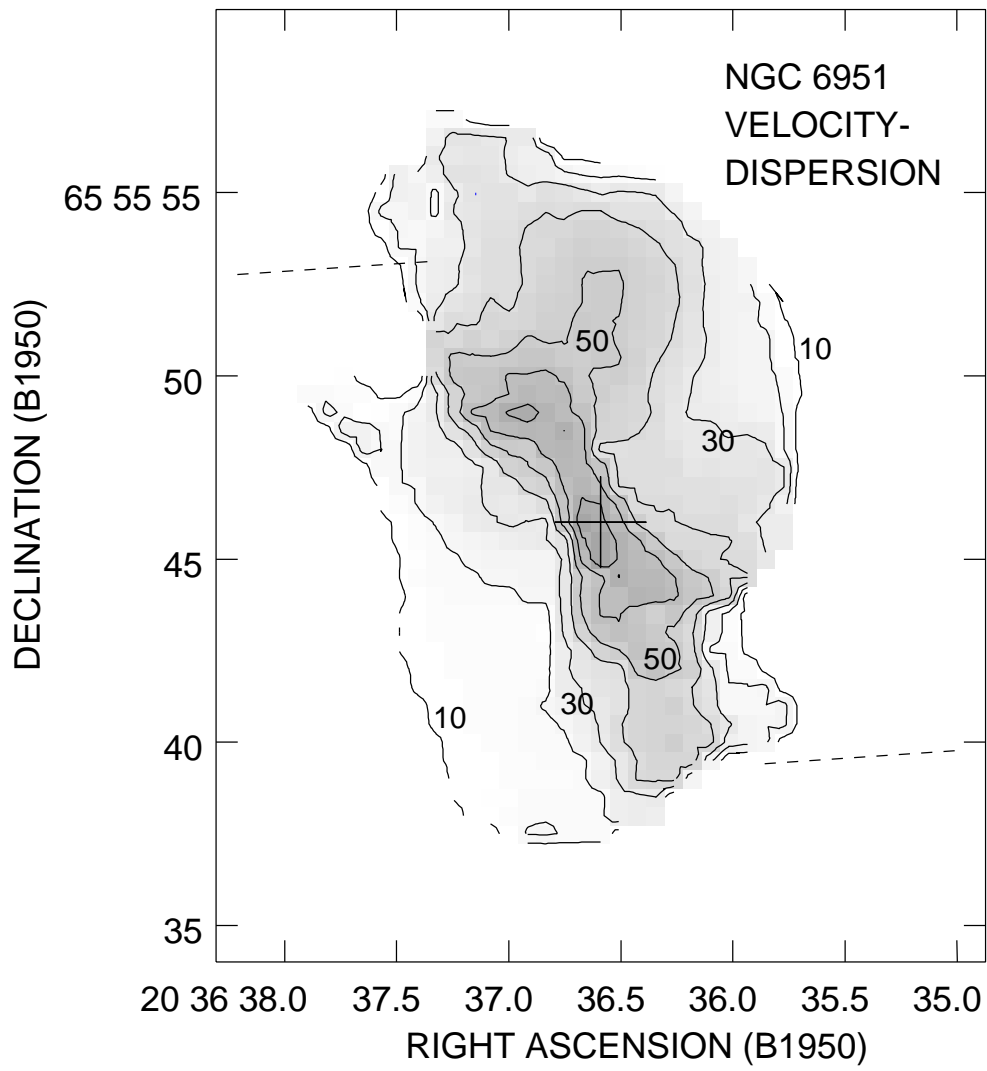
Kohno, Kawabe, and Vila-Vilaro 1998
Figure 12



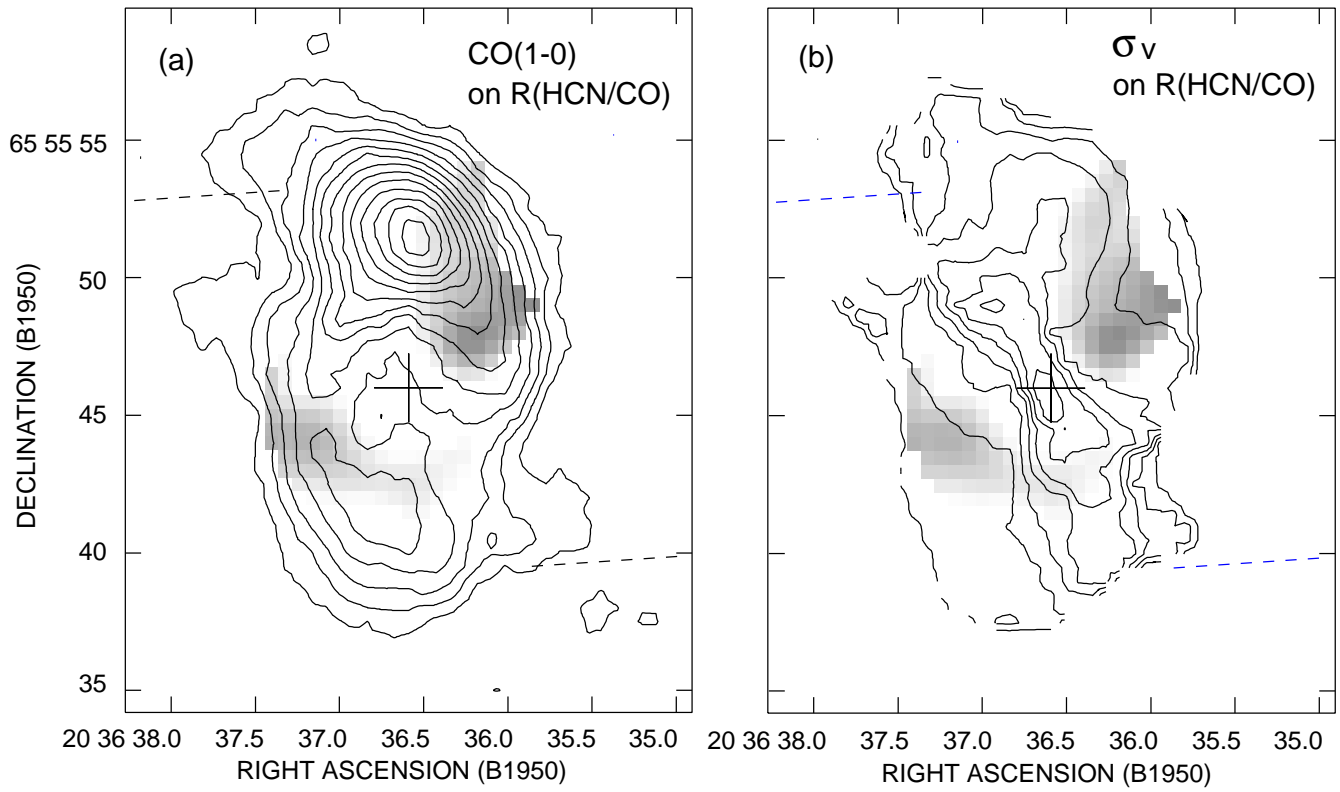
Kohno, Kawabe, Vila-Vilaro 1998
Figure 13



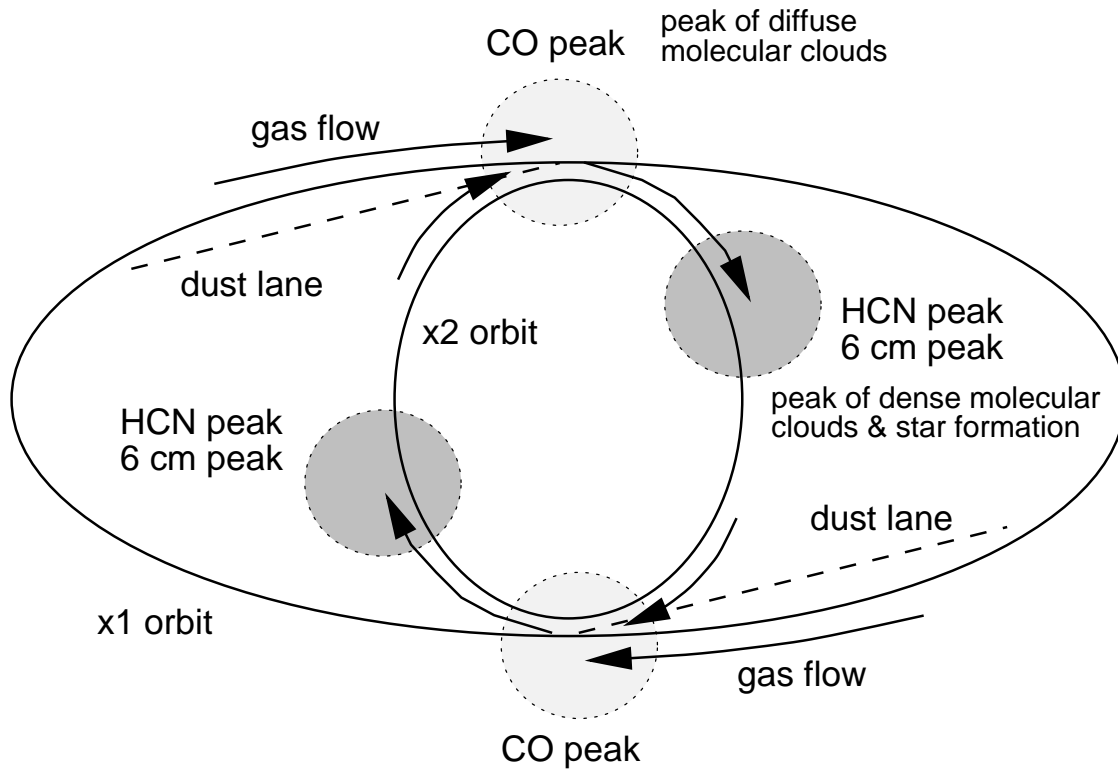
Kohno, Kawabe, and Vila-Vilaro 1998
Figure 14



Kohno, Kawabe, and Vila-Vilaro 1998
Figure 15



Kohno, Kawabe, and Vila-Vilaro 1998
Figure 16



Kohno, Kawabe, and Vila-Vilaro 1998
Figure 17